Oscillatory Magnetoresistance in Modulated Structures

題目

学位論文

Oscillatory Magnetoresistance in Modulated Structures

（変調構造下に於ける磁気抵抗の振動現象）

平成４年１２月　博士（理学）申請

氏名

東京大学大学院理学系研究科
物理学 専攻
八木 隆多

Ryuta Yagi

(1)

Thesis

Oscillatory Magnetoresistance in Modulated Structures

Ryuta Yagi

Institute for Solid State Physics
The University of Tokyo

December 1992

Preface

This thesis deals two phenomena concerned with modulated structures of the semiconductor samples.

In the former part of this thesis (Chapters 1-4) we deal with an angular dependent magnetoresistance oscillation (ADMRO) effect which originally has been discovered in organic compounds.

We have succeeded in a semiclassical interpretation of the ADMRO effect in the framework of the Boltzmann transport theory. It is demonstrated that the essential physics of the ADMRO effect is the difference of the asymptotic behavior of the magnetoresistance at the peak and valley angles. We have pointed out that the condition for the occurrence of the ADMRO effect is approximately given by $\omega_c\tau \sim 1$. We have also shown the ADMRO effect occurs principally in the transport perpendicular to the two-dimensional plane.

We have demonstrated the ADMRO effect in a tailored Fermi surface using the GaAs/AlGaAs superlattices. We have observed two or three peaks of the ADMRO in the vertical transport samples. The position of the peaks and its dependence on the carrier density strongly suggest that those peaks arise from ADMRO effect. The lateral transport properties, on the other hand, are featureless, which is consistent with our expectation.

It is known that some organic compounds exhibit an ADMRO effect with an inverted peak structure as compared with ordinary type. We have discussed this problem by calculating a magnetoresistance of some cylindrical Fermi surfaces with different corrugation symmetries. The ADMRO effect exhibits wide variation depending on the corrugation patterns, and some Fermi surface exhibit an inverted peak structure similar to the organic conductors. Although our caluclations explain some of the features of the inverted ADMRO effect, some features remain difficult to explain.

In the latter part of thesis (Chapters 5-6), we describe the oscillatory magnetoresistance of two-dimensional electron systems in modulated structures.

We have investigated energy spectra of two-dimensional electron systems in a periodically modulated magnetic field. Based on the calculated energy spectra, we infer an occurrence of the magnetoresistance oscillation similar to the oscillatory magnetoresistance in a periodic electric potential modulation (Weiss oscillation). It was found that the peaks and valleys of the present case are interchanged as compared with the Weiss oscillation. We also describe our attempt towards experimental observation of the effect using a GaAs/AlGaAs heterostructure with a striped ferromagnetic gate.

It should be mentioned that although the ADMRO effect in a quasi-two-dimensional systems and the Weiss oscillation in two-dimensional system are different in outlook, they share a common physical origin in that they both arise from a periodic quenching of the electron drift in a strong magnetic field at certain commensurability conditions.

Acknowledgements

I would like to express my gratitude to the thesis superviser, Prof. Y.Iye for valuable discussions and advices.

I have benefited greatly from kind help with semiconductor sample fabrication by Mr.Y.Hashimoto, Dr.T.Odagiri, Mr.H.Noguchi, Mr. M.Noguchi, Mr.H.Sakakibara, Dr. T.Saito, Prof. K.Hirakawa, Prof. H.Sakaki and Prof. T.Ikoma, of Institute of Industrial Science, University of Tokyo.

Help from the past and present members in the research group are gratefully acknowledged, with special mention to Dr.T.Osada, Dr.T.Tamegai, Mr.I.Oguro, Mrs.A.Fukushima, and Prof. S.Kagoshima.

I am further indebted to Prof.T.Takahashi and Mr.M.Hashimoto of ISSP for the characterization of superlattice samples by X-lay diffraction.

Finally, I would like to appreciate support from Japan Society for Promotion of Science.

Contents

List of Figures

List of Symbols and Abbreviations

θ: Polar angle measured from z axis. Often used for magnetic field orientation.
ϕ: Azimuthal angle in x-y plane. Often used for magnetic field orientation.
φ: Phase variable in Shockley tube integral.
ξ: Azimuthal angle in x-y plane. Often used for the azimuthal angle of k-vector.
E: Energy.
t: Interlayer transfer integral.
a: Interlayer distance.
k_α: α component of wave vector.
k_H: Wave vector component parallel to the magnetic field.
v_α: α component of group velocity.
$k_\parallel$: Tangential component of wave vector along the circumference of the electron orbit.
$v_\perp$: Group velocity perpendicular to magnetic field.
e: Unit charge.
e: Base of the natural logarithm.
$\hbar$: Plank constant.
m^*: Cyclotron mass.
m: Effective mass.
m_0: Free electron mass.
ω, ω_c: Cyclotron frequency.
ω_0 Cyclotron frequency at $\theta = 0°$. / Cyclotron frequency for $B = B_0$.
n_e: Carrier density.
τ: Relaxation time.
B_0: Uniform magnetic field.
B_1: Amplitude of magnetic field modulation.

μ_B Bohr magneton.
g: Electron g-factor.
$\rho_{\alpha\beta}$ Resistivity tensor components.
$\sigma_{\alpha\beta}$ Conductivity tensor components.
$[\sigma_{\alpha\beta}]_0$ Zeroth order term in the expansion of $\sigma_{\alpha\beta}$ in $1/\omega\tau$.
σ^s_{zz}: σ_{zz} for s-type Fermi surface corrugation.
σ^p_{zz}: σ_{zz} for s-type Fermi surface corrugation.
σ^{dxy}_{zz}: σ_{zz} for d_{xy}-type Fermi surface corrugation.
σ^{dxx}_{zz}: σ_{zz} for d_{xx}-type Fermi surface corrugation.

E_F: Fermi Energy.
k_F: Fermi wave number.
v_F: Fermi group velocity.

Bold face and the symbol $\vec{\ }$ are used to denote a vector.
$\mathbf{E}$: Electric field vector (E_x, E_y, E_z).
$\mathbf{B}$: Magnetic field vector $(B_x, B_y.B_z)$.
$\mathbf{v}$: Group velocity vector (v_x, v_y, v_z).
$\mathbf{k}$: Wave vector (k_x, k_y, k_z).
$\mathbf{J}$: Current.

$$\frac{\partial E}{\partial \mathbf{k}} \equiv \left(\frac{\partial E}{\partial k_x}, \frac{\partial E}{\partial k_y}, \frac{\partial E}{\partial k_z}\right).$$

$$\nabla T \equiv \left(\frac{\partial T}{\partial x}, \frac{\partial T}{\partial y}, \frac{\partial T}{\partial z}\right) \equiv \frac{\partial T}{\partial \mathbf{r}}.$$

$J_n(z)$: n-th order Bessel function.

n: Integer $1, 2, 3, \cdots$.
θ_n: n-th peak angle measured from $\theta = 0°$.
f^0: Fermi-Dirac distribution function at equilibrium.
f : Fermi-Dirac distribution function at steady state.
$\bar{v}_z$ Time averaged v_z over a cyclotron period.
ADMRO: Angular dependent magnetoresistance oscillation.
SdH: Shubnikov-de Haas effect.

Chapter 1
Introduction
The ADMRO Effect in Organic Conductors

1.1 Discovery of the ADMRO Effect

The research for the superconductivity in organic materials has brought about a wide variety of organic materials. Some of these have superconductivity but some of these do not. (BEDT-TTF) family is one of the most famous family of organic superconductors. One famous example is the κ-(BEDT-TTF)$_2$Cu(NCS)$_2$[1] whose superconducting transition temperature has first transcend 10 K.

Aside from the superconductivity, they often exhibit Shubnikov-de Haas (SdH) effect in low temperatures. The investigations of the SdH effect suggest that the Fermi surfaces for these materials are simple cylinder in shape. The cross-sectional area of the Fermi surface for these materials are successfully explained by band calculations[8].

Kajita *et al.*[2] have discovered a new phenomenon in a quasi-two-dimensional organic conductor θ-(BEDT-TTF)$_2$I$_3$. This material has a layered crystal structure and a large resistance anisotropy ~ 1000. The material exhibits a metallic behavior down to low temperatures and also undergoes a superconducting transition at about T =3.6K. Kajita *et al.* have found the magnetoresistance at low temperatures oscillates as a function of the angle of magnetic field measured from the direction perpendicular to the two-dimensional plane. Figure 1.1.1 shows the magnetic field angle dependence of the in-plane magnetoresistance in θ-(BEDT-TTF)$_2$I$_3$ for different field intensities. The oscillation is manifest. The angular dependent magnetoresistance oscillation effect has been also found independently by Kartsovnik *et al.*[3] in the same family of organic conductor, β-(BEDT-TTF)$_2$IBr$_2$.

The salient features of the oscillatory magnetoresistance can be summarized as follows:

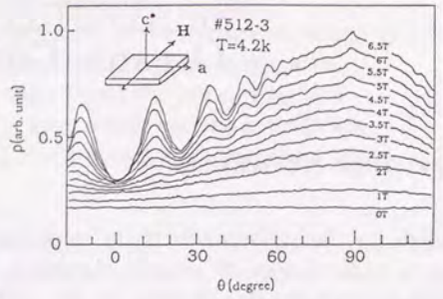

Fig 1.1.1 Angular dependence of the magnetoresistance of θ-(BEDT-TTF)$_2$I$_3$. (After Kajita *et al.* [2])

(1) When a magnetic field of fixed intensity is rotated within the plane perpendicular to the conductive two-dimensional sheet, the resistance shows oscillatory change with the field angle.

(2) The newly found oscillations are different from the SdH oscillations in that the oscillations occur as a function of the field angle, but not as a function of the field intensity. It can be observed even when no SdH effect is seen in the H-dependence of the magnetoresistance.

(3) The oscillations are periodic in $\tan\theta$, θ being the angle between the magnetic field and the direction normal to the two-dimensional plane. This is to be contrasted with a $1/\cos\theta$ dependence expected for the SdH effect for a quasi-two-dimensional Fermi surface.

(4) The oscillatory magnetoresistance appears for all azimuthal angle ϕ of the θ-rotation.

(5) The oscillations appear to be independent of the current direction with respect to the crystal axes.

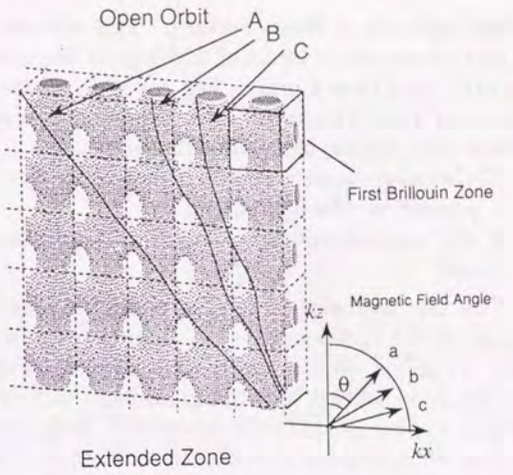

Fig. 1.2.1 Cylindrical Fermi surface elongating in k_z-direction with branches in k_x-direction. The open orbit **A** (**B**,**C**) occurs when the magnetic field is in **a** (**b**,**c**) direction, respectively. This occurs periodically in $\tan\theta$.

Prior to the discovery of the angular-dependent magnetoresistance oscillations, Kajita *et al.*[7] reported an anomalous linear H-dependence of the magnetoresistance in this system.

1.2 Fermi Surface Topology

The measurement of magnetoresistance as a function of magnetic field angle often provides us the information on the shape of the Fermi surface[4]. In some cases, the shape of the Fermi surface can be determined.

From a semiclassical point of view, the electron motion in a magnetic field is described by a following equation of motion:

$$\hbar\frac{d\mathbf{k}}{dt} = e\mathbf{v}\times\mathbf{B}. \tag{1.2.1}$$

The Lorentz force changes the k-vector of an electron on the Fermi surface, in the direction perpendicular to **B** and **v**. It defines an

electron orbit on a Fermi surface. This electron orbit is classified into two categories in terms of topology of the orbital shape, namely, open orbit and closed orbit. The topology of the Fermi surface can be inferred from the asymptotic behavior of magnetoresistance for different field angles, using the following rule:

[a] If the magnetoresistance is divergent as $H \to \infty$, the open orbit is present for the field angle.

[b] If the magnetoresistance tends to saturate, all the orbits are closed.

The first explanation for the ADMRO effect was sought in the topology of the Fermi surface *i.e.* angular periodic occurrence of open orbits. It seems we can construct a plausible Fermi surface using a extended zone scheme by adding branches to a cylinder for the open orbits to appear periodically in $\tan\theta$ [3] as illustrated in Fig. 1.2.1. However we encounter a trouble to construct a Fermi surface which satisfies a following experimental results. The measurement of the angular dependence of resistance by a two-axis (θ,ϕ) rotation of magnetic field does not cause a sudden change of the occurrence of the peaks. Here, ϕ is the azimuthal angle defined in Fig. 1.2.2. The peak angle θ_n of the ADMRO for given ϕ changes continuously in ϕ rotation. The peak of the ADMRO never suddenly appear or disappear in ϕ rotation. If the peak arises from the occurrence of the open orbit, the peak angles are restricted in a narrow regime. Thus the origin for the oscillation must be sought in other causes.

1.3 Yamaji's theory

The key to the understanding of the phenomenon was first given by Yamaji[5]. The angular dependence of the SdH effect suggests that the family of organic conductors have a corrugated cylindrical Fermi surface. The electronic state for these materials is often described, to a first approximation, by the following simple energy dispersion relation,

$$E = \frac{\hbar^2}{2m}(k_x^2 + k_y^2) - 2t\cos(ak_z). \qquad (1.3.1)$$

Here, E is the energy, m is the effective mass, $k_{x(y)}$ is the $x(y)$ component of k vector , t is the interlayer transfer integral and a is a interlayer distance. Yamaji has shown that the area, $S_k(k_0)$, of a

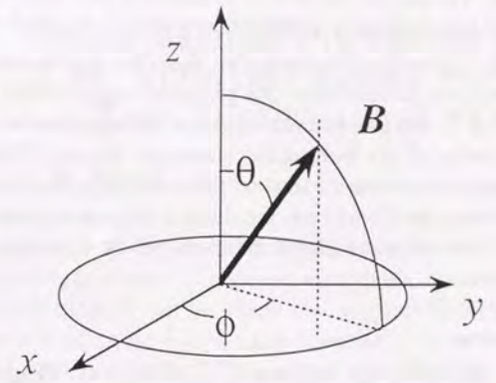

Fig.1.2.2 Schematic diagram of two-axis magnetic field rotation.

cross-section of Fermi surface defined by the plane perpendicular to the field direction is given by

$$S_k(k_0) = [\pi k_F^2 + 4\pi mt\cos(ak_0)J_0(ak_F\tan\theta) + O(t^2)]/\cos\theta. \quad (1.3.2)$$

Here, $J_0(z)$ is the zero-th order Bessel function and k_0 is a variable that specifies a particular cross-section. (See Fig. 2.3.1 in the next section.) The cross-sectional area $S_k(k_0)$ generally has a dispersion as a function of the variable k_0 due to the presence of the corrugation. Yamaji has pointed out that at special angles given by

$$ak_F\tan\theta_n = (n - 1/4)\pi \qquad n : \text{integer}, \qquad (1.3.3)$$

$S_k(k_0)$ takes a single value independent of k_0, namely the dispersion of $S_k(k_0)$ vanishes. Eq.(1.3.3) has given a natural explanation for the periodicity in $\tan\theta$ of the observed ADMRO. A nearly complete quantization occurs for this angles. Yamaji has discussed the oscillation in the light of the localization effect arising from the nearly complete quantization. Based on the Yamaji's model, Osada *et al.*[6] has made a numerical calculation of the quantum mechanical energy eigenvalues.

1.4 Organization

Although Yamaji succeeded in explaining the $\tan\theta$ dependence, the origin of the oscillatory magnetoresistance remained unclear.

In the following Chapters, we describe our theoretical and experimental efforts to elucidate the physical origin of the ADMRO effect. In Chapter 2, we present semiclassical interpretation of the ADMRO effect in terms of the Boltzmann transport theory. Chapter 3 describes the experimental observation of the ADMRO effect in GaAs/AlGaAs superlattices. In Chapter 4, we discuss the anomalous ADMRO effect with an inverted peak structure observed in a certain class of organic conductors.

References

1) H. Urayama, H. Yamochi, G. Saito, K. Nozawa, T. Sugano, M. Kinoshita, S. Sato, K. Oshima, A. Kawamoto and J. Tanaka: Chem. Lett.**1988**(1988)55.
2) K. Kajita, Y. Nishio, T. Takahashi, W. Sasaki, R. Kato, H. Kobayashi, A. Kobayashi and Y. Iye: Solid State Commun., **70**(1989)1189.; K. Kajita, Y. Nishio, T. Takahashi, W. Sasaki, R. Kato, H. Kobayashi, A. Kobayashi and Y. Iye: *"Physics and Chemistry of Organic Superconductors"*, *eds.* G. Saito and S. Kagoshima, (Springer-Verlag, Heidelberg, 1990) p.212.
3) M. V. Kartsovnik, P. A. Kononovich, V. N. Laukhin and I. F. Schegolev: Sov. Phys. JETP Lett., **48**(1988)541.
4) (for example) N.W.Ashcroft and N.D.Mermin: *"Solid State Physics"*, CBS Publishing Asia LTD., (Philadelphia) p.234.
5) K. Yamaji: J. Phys. Soc. Jpn., **58**(1989)1520.
6) T. Osada, R. Yagi, S. Kagoshima, N. Miura, M. Oshima, and G. Saito: *"Physics and Chemistry of Organic Superconductors"*, *eds.* G. Saito and S. Kagoshima, (Springer-Verlag, Heidelberg, 1990) p.220.
7) K. Kajita, Y. Nishio, T. Takahashi, W. Sasaki, R. Kato, H. Kobayashi and A. Kobayashi: Solid State Commun., **70**(1989)1181.
8) K. Oshima, T. Mori, H. Inokuchi, H. Urayama, H. Yamochi and G. Saito: Phys. Rev., **B38**(1988) 938.

Chapter 2

Semiclassical Interpretation of The ADMRO Effect in Quasi-Two-Dimensional Systems

Calculation of magnetoresistance in quasi-two-dimensional systems is carried out in the framework of the Boltzmann transport theory in an attempt to understand angular dependent oscillatory magnetoresistance phenomea discovered in organic conductors. Calculated magnetoresistance curves show the angular dependent oscillations reminiscent of those found experimentally. It is argued that the essential physics underlying the resistance oscillations lies in the angular dependence of the high field asymptotic behavior (saturation *vs.* divergence) of semiclassical magnetoresistance which arises from Fermi surface topology.

2.1 Introduction

As seen in the previous Chapter, although Yamaji has succeeded in the explanation of the θ-dependence of the ADMRO effect, the origin of the ADMRO effect was still unclear. In this work, we present a semiclassical picture based on a Boltzmann transport theory, which gives a natural explanation for the angular dependent magnetoresistance oscillation (ADMRO) effect.

This Chapter is organized as follows. In the next section we describe the Shockley tube integral formula for the calculation of the magnetoconductity in the Boltzmann transport theory. In Section 2.3, we define a model to be discussed. In Sec. 2.4, we describe numerical calculation of magnetoresistance. In Sec. 2.5, we describe the analytical calculation of the magnetoconductivity. Sec. 2.6 is devoted to summary and concluding remarks.

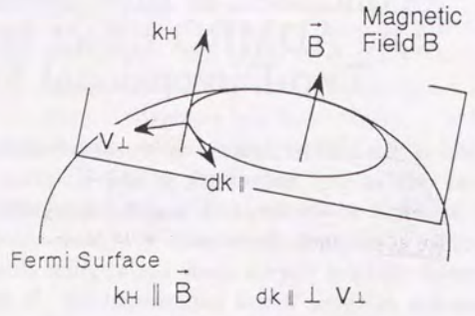

Fig.2.2.1 Schematic diagram of the Fermi surface.

2.2 Shockley Tube Integral[5)]

We start with the Boltzmann equation for the steady state distribution function $f(\mathbf{k},\mathbf{r},t)$:

$$e\left(-\frac{\partial f^0}{\partial E}\right)\mathbf{E}\cdot\mathbf{v_k} = \frac{g_\mathbf{k}}{\tau} + \frac{e}{\hbar}(\mathbf{v_k}\times\mathbf{B})\cdot\left(\frac{\partial g_\mathbf{k}}{\partial \mathbf{k}}\right). \\ = \frac{g_\mathbf{k}}{\tau} + \frac{\partial g_\mathbf{k}}{\partial t}. \tag{2.2.1}$$

Here, f^0 is a distribution function for equilibrium, $g_\mathbf{k}$ is defined by $g_\mathbf{k} = f_\mathbf{k} - f^0_\mathbf{k}$, $\mathbf{E}$ is an electric field and τ is a relaxation time. Using the variables illustrated in Fig.2.2.1, the equation of motion can be written in the following form,

$$dk_\parallel = \frac{e}{\hbar}v_\perp B dt. \tag{2.2.2}$$

Here, $v_\perp$ is the group velocity component perpendicular to the magnetic field and $k_\parallel$ is the tangential component of the k-vector along

the circumference of the electron orbit. The time period T is written as

$$\mathrm{T} = \oint \frac{\hbar/e}{v_\perp B} dk_\parallel. \tag{2.2.3}$$

The cyclotron frequency ω and the cyclotron mass m^* are defined by

$$\omega \equiv \frac{2\pi}{\mathrm{T}} = \frac{eB}{m^*}, \tag{2.2.4}$$

$$m^* = \frac{\hbar}{2\pi}\oint \frac{dk_\parallel}{v_\perp}. \tag{2.2.5}$$

We define a phase variable φ by

$$d\varphi = \omega dt. \tag{2.2.6}$$

By use of above formulae,

$$\frac{\partial g}{\partial t} = \dot{\varphi}\frac{\partial g}{\partial \varphi} = \omega\frac{\partial g}{\partial \varphi}, \tag{2.2.7}$$

then eq.(2.2.1) becomes

$$e\left(-\frac{\partial f^0}{\partial E}\right)\mathbf{E}\cdot\mathbf{v_k} = \frac{g}{\tau} + \omega\frac{\partial g}{\partial \varphi} \\ = \omega \mathrm{e}^{-\varphi/\omega\tau}\frac{\partial}{\partial\varphi}(\mathrm{e}^{\varphi/\omega\tau} g). \tag{2.2.8}$$

Eq.(2.2.8) can be transformed into an integral formula,

$$g(E,k_H,\varphi) = \frac{e}{\omega}\left(-\frac{\partial f^0}{\partial E}\right)\int_{-\infty}^{\varphi} d\varphi' \exp\{(\varphi'-\varphi)/\omega\tau\}\mathbf{v_k}(E,k_H,\varphi')\cdot\mathbf{E}. \tag{2.2.9}$$

Here k_H is the k-vector component parallel to the magnetic field. The current $\mathbf{J}$, on the other hand, is given by the following formula

$$\mathbf{J} = 2\int e\mathbf{v_k} g_\mathbf{k}\frac{d^3k}{(2\pi)^3} = \frac{e}{4\pi^3}\int dE\int dk_H\int_0^{2\pi} d\varphi\left\{\frac{m^*}{\hbar^2}\mathbf{v_k} g_\mathbf{k}\right\}. \tag{2.2.10}$$

Here, we used

$$d^3k = dk_x dk_y dk_z = dk_H dk_\perp dk_\parallel = \frac{m^*}{\hbar^2} dk_H d\varphi dE,$$

$$\hbar v_\perp dk_\perp = \hbar\left(\frac{1}{\hbar}\frac{dE}{dk_\perp}\right)dk_\perp = dE,$$

$$dk_\parallel = ev_\perp B dt = \frac{ev_\perp B}{\omega} d\varphi = \frac{m^* v_\perp}{\hbar} d\varphi. \quad (2.2.11)$$

The conductivity tensor components can be obtained by substituting eq.(2.2.9) into eq.(2.2.10).

$$\sigma_{\alpha\beta} = \frac{e^2}{4\pi^3\hbar^2}\int dE\left(-\frac{\partial f^0}{\partial E}\right)\int dk_H \int_0^{2\pi} d\varphi \int_0^{+\infty} d\varphi' \; v_\alpha(\varphi, k_H, E)\, v_\beta(\varphi - \varphi', k_H, E)\frac{m^*}{\omega}\, e^{-\varphi'/\omega\tau}. \quad (2.2.12)$$

For $k_B T \ll E_F$, the magnetoconductivity tensor components are approximated by

$$\sigma_{\alpha\beta} = \frac{e^2}{4\pi^3\hbar^2}\int dk_H \int_0^{2\pi} d\varphi \int_0^{+\infty} d\varphi' \; v_\alpha(\varphi, k_H, E_F)\, v_\beta(\varphi - \varphi', k_H, E_F)\frac{m^*}{\omega}\, e^{-\varphi'/\omega\tau}. \quad (2.2.13)$$

Eq.(2.2.12) or (2.2.13) is called Shockley tube integral.

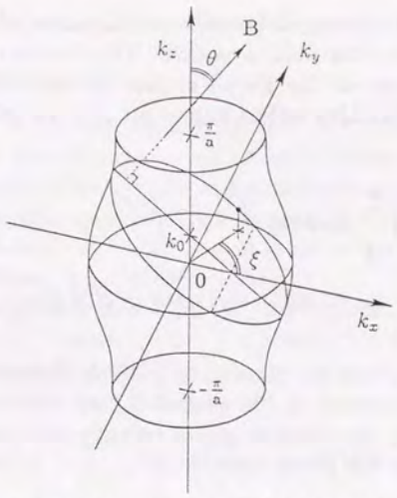

Fig.2.3.1 Schematic diagram of the Fermi surface of the model quasi-two-dimensional system.

2.3 Model

Both large resistance anisotropy (~ 1000) and band calculations indicate a two-dimensional character of the electronic structure of the organic compounds,θ-(BEDT-TTF)$_2$I$_3$ *etc.* We consider a quasi-two-dimensional Fermi surface expressed by the energy dispersion relation given by eq.(1.3.1). We restrict ourselves to a case, $t \ll E_F$, which corresponds to the weak corrugation limit. The Fermi surface is a weakly corrugated cylinder as depicted in Fig.2.3.1.

Based on the band model, we study the magnetoconductivity tensor components by use of the Shockley tube integral numerically as well as analytically. The integral is taken over closed orbits in the extended zone scheme. The conductivity tensor components are calculated as a function of the tilt angle θ of the magnetic field from the z-axis. We take the plane of the field rotation as the zx-plane. It is convenient to introduce a variable k_0 (see Fig.2.3.1) which satisfies the following relation:

$$k_0 = k_z + k_x \tan\theta. \quad (2.3.1)$$

This variable k_0 serves as an index of the slices of the Fermi surface perpendicular to the field direction. The electron trajectory follows the circumference of the Fermi surface on each slice. Using this k_0 variable, the Shockley tube integral for a given field angle is written as

$$\sigma_{\alpha\beta} = \frac{e^2}{4\pi^3\hbar^2}\int_{-\frac{\pi}{a}}^{\frac{\pi}{a}} \cos\theta dk_0 \int_0^{2\pi} d\varphi \int_0^{+\infty} d\varphi' \\ v_\alpha(\varphi, k_H)\, v_\beta(\varphi-\varphi', k_H)\frac{m^*}{\omega}\, e^{-\varphi'/\omega\tau}. \quad (2.3.2)$$

For a field angle not too close to $\pi/2$, all the electron orbits are closed and singly connected in the extended zone scheme. For the closed electron orbits, the electron group velocity has the periodicity of 2π with respect to the phase variable φ:

$$v_\alpha(\varphi + 2\pi) = v_\alpha(\varphi). \quad (2.3.3)$$

Using this periodicity, the upper limit for the integration over φ' can be reduced from ∞ to 2π, to yield

$$\sigma_{\alpha\beta} = \frac{e^2}{4\pi^3\hbar^2}\int_{-\frac{\pi}{a}}^{\frac{\pi}{a}} dk_0 \left\{ \frac{\cos\theta}{1-e^{-2\pi/\omega\tau}} \int_0^{2\pi} d\varphi \int_0^{2\pi} d\varphi' \right. \\ \left. v_\alpha(\varphi, k_H) v_\beta(\varphi-\varphi', k_H)\frac{m^*}{\omega} e^{-\varphi'/\omega\tau} \right\}. \quad (2.3.4)$$

2.4 Numerical Calculation of the Magnetoresistance

2.4.1 Method of Numerical Integration

We briefly sketch the outline of the numerical integration of eq.(2.3.4). First we calculate a set of co-ordinates (typically 512 points) of the circumference of the Fermi surface cross-section perpendicular to the magnetic field. Using eqs.(2.2.4)-(2.2.6), we calculate the phase variable φ, the cyclotron mass m^* as a function of k_0, and group velocity v_α as a function of φ.

Fourier expansion is used to obtain the correlation function of v_α and v_β in eq.(2.3.4). Since $v(\varphi)$ has the periodicity, $v(\varphi) = v(\varphi+2\pi)$, we expand $v(\varphi)$ in a Fourier series,

$$v_\alpha(\varphi) = \sum_{n=0}^{\infty}\Big(a_n\cos(n\varphi) + b_n\sin(n\varphi)\Big), \\ v_\beta(\varphi) = \sum_{n=0}^{\infty}\Big(c_n\cos(n\varphi) + d_n\sin(n\varphi)\Big). \quad (2.4.1)$$

Then the correlation function in eq.(2.3.4) can be reduced formally, to yield

$$\sigma_{\alpha\beta} = \frac{e^2\tau\cos\theta}{2\pi^2\hbar^2}\int dk_0 m^*\left\{ a_0c_0 \right. \\ \left. + \frac{1}{2}\sum_{n=1}^{\infty}\left\{ \frac{(a_nc_n + b_nd_n)}{1+(\omega\tau n)^2} - \frac{(a_nd_n - b_nc_n)\omega\tau n}{1+(\omega\tau n)^2} \right\} \right\}. \quad (2.4.2)$$

A set of group velocity for equally spaced φ values (2^N) is computed by interpolation. We calculate the Fourier coefficients by a fast Fourier transform (FFT) technique.

Then integration of eq.(2.4.2) is achieved by summation. We calculate the all independent components of the magnetoconductivity tensor. The resistivity tensor was then obtained by tensor inversion.

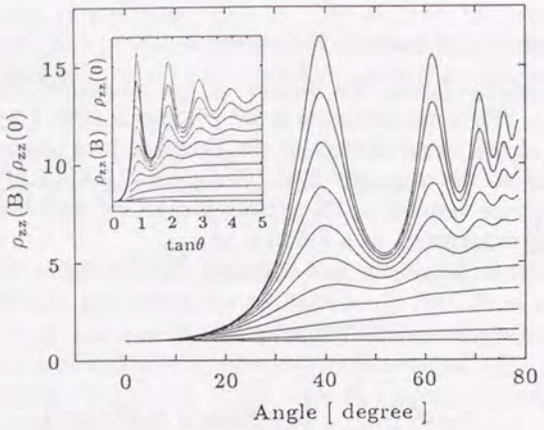

Fig.2.4.1 Angular dependence of the zz component of the resistivity tensor for different magnetic fields. From top to bottom, the value of $\omega_0\tau$ varies from 4 to 0 with 0.4 step. The inset is the replot against $\tan\theta$. The parameter values are $E_F/t = 100$ and $mta^2/\hbar^2 = 0.045$.

2.4.2 Results of the Numerical Calculation

Figure 2.4.1 shows the numerical result of ρ_{zz} for different values of $\omega_0\tau$, where $\omega_0 = eB/m$ is the cyclotron frequency for $\theta = 0$. The parameter values for this figure are $E_F/t = 100$ and $mta^2/\hbar^2 = 0.045$ and are chosen to approximately reproduce the Fermi surface of the BEDT-TTF salts. The calculated ρ_{zz} shows oscillations for $\omega_0\tau > 1$. Note that for a given $\omega_0\tau$ value, $\omega\tau(\approx \omega_0\tau\cos\theta)$ diminishes as θ is increased. Inset of Fig. 2.4.1 is a replot of the ρ_{zz} curves as a function of $\tan\theta$. It is seen that the oscillations are periodic in $\tan\theta$, with a period $\Delta(\tan\theta) = 1.05$. This period agrees with the formula as first derived by Yamaji.

Next we look at the same phenomenon as a function of magnetic field at fixed angles. Figure 2.4.2 shows the traces of $\rho_{zz}(B)$ at three

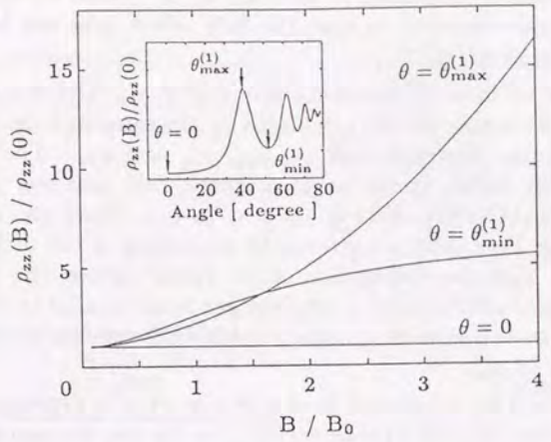

Fig. 2.4.2 Magnetic field dependence of the zz component of the resistivity tensor at fixed angles. Here, $B/B_0 = \omega_0\tau(= eB\tau/m)$. The positions of $\theta^{(1)}_{min}$ and $\theta^{(1)}_{max}$ are indicated in the inset. The parameter values are the same as in Fig. 2.4.1

different angles: $\theta = 0$, $\theta^{(1)}_{\rm max}$, and $\theta^{(1)}_{\rm min}$ as indicated in the inset. At $\theta = 0$, ρ_{zz} is constant because the zz component of the group velocity does not change with field for this field direction. It is noted that the high field magnetoresistance behavior is quite distinct for $\theta = \theta^{(1)}_{\rm max}$ and $\theta = \theta^{(1)}_{\rm min}$. While ρ_{zz} for $\theta = \theta^{(1)}_{\rm max}$ shows no sign of saturation, that for $\theta = \theta^{(1)}_{\rm min}$ saturates rather quickly. This angular dependence of the asymptotic behavior of the semiclassical magnetoresistance is the origin of the ADMRO.

The amplitude of ADMRO increases with increasing $\omega\tau$. Since the Landau level quantization is not taken into account in the present semiclassical model, the $\rho_{zz}(B)$ curves in Figs. 2.4.1 and 2.4.2 do not show the SdH oscillations. In an actual experiment, the SdH oscillations becomes increasingly prominent as $\omega\tau$ is increased, and will dominate the ADMRO effect. Although the two effects can be

discriminated in principle, it is desirable to choose an appropriate experimental condition so that the SdH effect does not hinder the observation of ADMRO.

So far we have discussed the behavior of ρ_{zz}. Other components of resistivity tensor can be calculated by the same method. Fig.2.4.3 shows angular dependence of ρ_{xx},ρ_{yy}, ρ_{xy} and ρ_{yx}. The ADMRO effect is not visible in the same magnetic field intensity as in Fig. 2.4.1 while ADMRO effect is eminent in ρ_{zz}. Since the oscillation stems from a periodic occurrence of quenching of the drift velocity associated with the corrugation of the Fermi surface, the oscillation in the lateral conductivity coefficient are much smaller in magnitude around $\omega_0\tau \sim 1$ so that we observe ADMRO principally in ρ_{zz} and not in ρ_{xx} or ρ_{xy}.

It should be mentioned that in Kajita *et al.*'s experiment[1)], the nominal direction of the probe current is in the two-dimensional plane, so that ρ_{xx} and ρ_{yy} are supposed to be the measured quantities. Taken literally, this result is in contradiction with our calculation. However, we speculate that, considering the large conductivity anisotropy in these materials, it is not unlikely that the nominal basal plane resistivity contains some ρ_{zz} component depending on the actual electrode configuration and the current path.

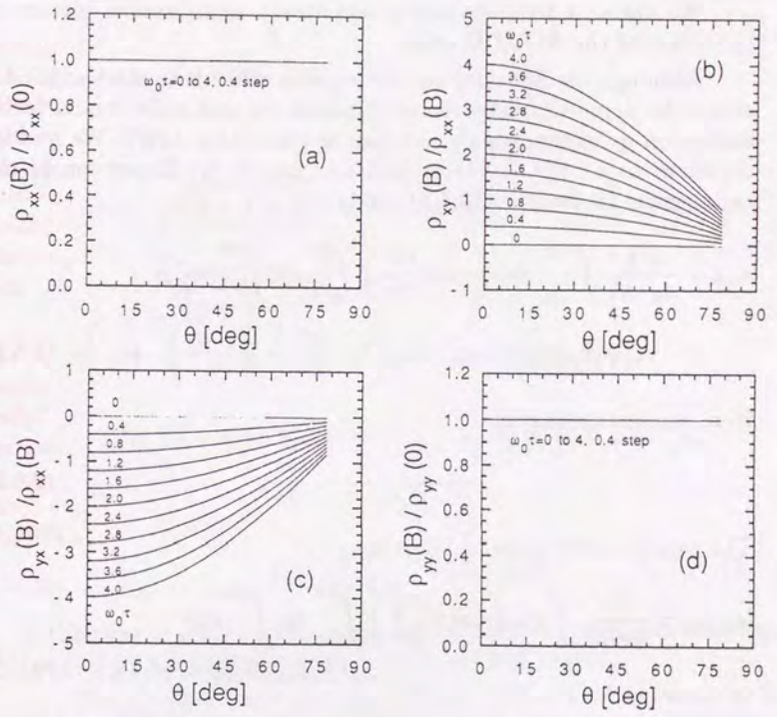

Fig. 2.4.3 Angular dependence of (a)ρ_{xx}, (b)ρ_{xy}, (c)ρ_{yx} and (d) ρ_{yy}. The parameter values are the same as Fig.2.4.1

2.5 Analytical Results

2.5.1 Pictorial Explanation of the ADMRO Effect

We derive a few relations to describe a semiclassical picture of the origin of the ADMRO effect.

Although the Shockley tube integral is difficult to solve explicitly except for some simplified Fermi surfaces, we can make a qualitative discussion by expanding the integral in $1/\omega\tau$, (*i.e.* $1/B$). We restrict ourselves to a high magnetic field *i.e.* $\omega\tau \gg 1$. Expansion of the exponential factor in eq.(2.4.5) yields

$$\sigma_{\alpha\beta} = \frac{e^2\tau}{4\pi^3\hbar^2}\int_{-\pi/a}^{\pi/a} dk_0\left(\cos\theta\frac{m^*}{2\pi}\right)\int_0^{2\pi} d\varphi\int_0^{2\pi} d\varphi' \\ v_\alpha(\varphi,k_H)v_\beta(\varphi-\varphi',k_H)\left\{1-\frac{\varphi'}{\omega\tau}+\frac{1}{2}\left(\frac{\varphi'}{\omega\tau}\right)^2+\ldots\right\}. \quad (2.5.1)$$

Here, we approximated

$$\frac{1}{1-e^{-2\pi/\omega\tau}} \sim \frac{\omega\tau}{2\pi}. \quad (2.5.2)$$

The zero-th order term in $1/\omega\tau$ is

$$[\sigma_{\alpha\beta}]_0 = \frac{e^2\tau}{4\pi^3\hbar^2}\int dk_0\left(\cos\theta\frac{m_H^*}{2\pi}\right)\int_0^{2\pi} d\varphi\int_0^{2\pi} d\varphi' \\ v_\alpha(\varphi,k_H)\, v_\beta(\varphi-\varphi',k_H). \quad (2.5.3)$$

This term determines the conductivity in the high field limit because the other terms in eq.(2.5.1) are higher order in $1/\omega\tau$.

The conductivity component given by eq.(2.5.3) arises from electron drift motion in the high field limit. Eq.(2.5.3) is written as

$$\int_0^{2\pi} d\varphi\int_0^{2\pi} d\varphi'\left\{v_\alpha(\varphi)v_\beta(\varphi-\varphi')\right\} \\ = \left\{\int_0^{2\pi} v_\alpha(\varphi)d\varphi\right\}\left\{\int_0^{2\pi} v_\beta(\varphi-\varphi')d\varphi'\right\} \quad (2.5.4) \\ = \left\{\int_0^{2\pi} v_\alpha(\varphi)d\varphi\right\}\left\{\int_0^{2\pi} v_\beta(\varphi)d\varphi'\right\},$$

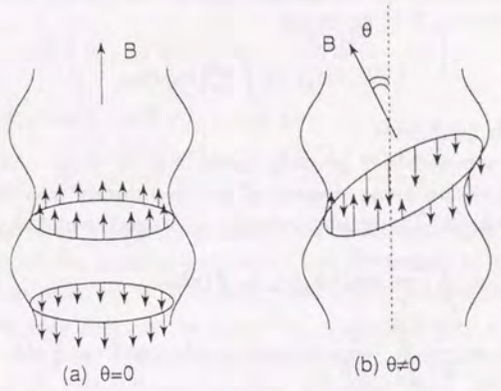

Fig.2.5.1 The behavior of v_z for (a)$\theta = 0$ and (b) $\theta \neq 0$.

and

$$\bar{v}_\alpha = \frac{1}{2\pi}\left\{\int_0^{2\pi} v_\alpha(\varphi)d\varphi\right\} \quad (2.5.5)$$

is the time average of the group velocity since φ is proportional to t (eq.(2.2.6)), which goes from 0 to 2π for one period.

The physical origin for the ADMRO effect is understood by the drift motion picture. We consider the electron drift in z-direction. We first consider the case of $\theta = 0°$.($H \parallel z$.) Fig.2.5.1-(a) illustrates v_z of a certain point in the electron orbit for $\theta = 0$. The z-component of the group velocity,

$$v_z = \frac{1}{\hbar}\left(\frac{\partial E}{\partial k_z}\right) = \frac{2ta}{\hbar}\sin(ak_z) \quad (2.5.6)$$

does not change during a cyclotron motion. The drift velocity is

$$\bar{v}_z = \frac{1}{2\pi}\int_0^{2\pi}\frac{2ta}{\hbar}\sin(ak_0)d\varphi = \frac{2ta}{\hbar}\sin(ak_0). \quad (2.5.7)$$

Thus, the z-component of the electron drift velocity has a finite dispersion as a function of k_0. This leads to a finite conductivity along the z-direction. It is given by

$$\sigma_{zz} \propto \int \bar{v}_z^2(k_0) dk_0, \tag{2.5.8}$$

in the high field limit.

Next we consider general cases, *i.e.* $\theta \neq 0$. As illustrated in Fig.2.5.1-(b) the z-component of group velocity oscillates during cyclotron motion. The group velocity averaged over the trajectory is

$$\begin{aligned} \bar{v}_z &= \oint \frac{2ta}{\hbar} \sin(ak_z(\varphi, k_0, \theta)) d\varphi \\ &= \frac{1}{2\pi} \int_o^{2\pi} \frac{2ta}{\hbar} \sin(ak_0 - ak_F \tan\theta \cos\xi) d\varphi. \end{aligned} \tag{2.5.9}$$

Here, we used $(k_x, k_y) = (k\cos\xi, k\sin\xi)$ and $k^2 = k_x^2 + k_y^2$. Analytical integration of eq.(2.5.9) for a general case is not easy because of a complicated dependence of k and ξ on φ. For $(t/E_F) \ll 1$, we can approximate the phase variable φ by ξ, and we replace k by k_F (Appendix A). Then eq.(2.5.9) becomes

$$\begin{aligned} \bar{v}_z &= \frac{1}{2\pi} \int_0^{2\pi} d\varphi \left\{ \frac{2ta}{\hbar} \sin(ak_0 - ak_F \tan\theta \cos\varphi) \right\} \\ &= \frac{2ta}{\hbar} \sin(ak_0) \left\{ \frac{1}{2\pi} \int_0^{2\pi} d\varphi \cos(ak_F \tan\theta \cos\varphi) \right\} \quad (2.5.10) \\ &= \frac{2ta}{\hbar} J_0(ak_F \tan\theta) \sin(ak_0). \quad (2.5.11) \end{aligned}$$

Recalling that $J_0(z)$ is approximated for $z > 1$ by

$$J_0(z) \approx \sqrt{\frac{2}{\pi z}} \cos(z - \frac{\pi}{4}), \tag{2.5.12}$$

the *zeros* occur at

$$ak_F \tan\theta = (n - \frac{1}{4})\pi. \tag{2.5.13}$$

When the field angle satisfy the above condition, the electron drift vanishes for all values of k_0. The periodic occurrence of such quenching of the drift motion leads to the ADMRO effect.

2.5.2 The ADMRO Effect in Vertical Transport

The final result for σ_{zz} in the approximation is written as follows:

$$\sigma_{zz} = \sigma_{zz}^0 \left\{ J_0^2(A) + 2 \sum_{\nu=1}^{\infty} \frac{J_\nu^2(A)}{1 + (\omega_0 \tau \nu \cos\theta)^2} \right\}, \tag{2.5.14}$$

where $A = ak_F \tan\theta$, and σ_{zz}^0 given by

$$\sigma_{zz}^0 = \frac{2e^2 m t^2 a \tau}{\pi \hbar^4} = \left(\frac{\tilde{v}_z}{v_F} \right)^2 \frac{n_e e^2 \tau}{m} \tag{2.5.15}$$

is the conductivity along the z-direction in the absence of magnetic field. Here n_e is the number density of the electrons, and $\tilde{v}_z = 2ta/\hbar$. The derivation of eq.(2.5.14) is described in Appendix A.

Here, we only discuss the meaning of eq.(2.5.14). First we note that $\rho_{zz} \sim 1/\sigma_{zz}$ for a quasi-two-dimensional electron system. The terms with $\nu \geq 1$ in the summation diminish with increasing field strength (increasing $\omega_0\tau$). The conductivity in the high field limit ($\omega_0\tau \longrightarrow \infty$) is therefore governed by $J_0(A)$.

This term arise from the electron drift motion discussed in Sec. 2.5.1. The term becomes negligible when the angle θ satisfies the condition, eq.(2.5.13). For these values of θ, σ_{zz} vanishes in the high field limit, and $\rho_{zz}(\sim 1/\sigma_{zz})$ diverges. For other values of θ, σ_{zz} remains finite so that ρ_{zz} becomes saturated at high fields. The anaytical results for $\rho_{zz}(\theta) \sim 1/\sigma_{zz}$ with σ_{zz} given by eq.(2.5.14) actually agree very well with the numerically obtained curves shown in Figs. 2.4.1 and 2.4.2, indicating that the replacement of φ of ξ employed in the analytic calculation is a good approximation.

The decrease of the $\nu \geq 1$ terms at higher field becomes less rapid for a larger value of θ because of the $\cos\theta$ factor in the denominator. This corresponds to the obvious fact that as θ increases, the same value of $\omega\tau$ requires a progressively higher field. Thus, for a given value of $\omega_0\tau$ as in Fig. 2.4.1, the ρ_{zz} maxima are less pronounced at higher angles. Turning to the ρ_{zz} minima, because the peak value of $J_0(z)$ decreases with increasing z, the maximum of σ_{zz} decreases with increasing θ. This means that the saturation value of ρ_{zz} in the high field limit increases with θ. The above two arguments give an explanation for the decrease of the amplitude of the angular dependent oscillations with increasing θ.

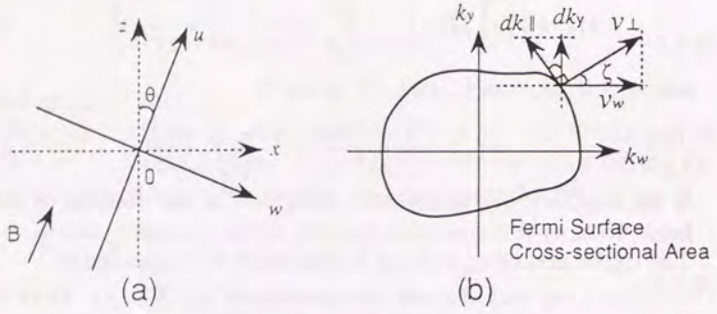

Fig 2.5.2 (a)Schematic diagram of the u- and w-axes.
(b) Definition of ζ.

2.5.3 On the Lateral Transport Coefficients

As mentioned in Sec. 2.4, the ADMRO effect in the lateral transport coefficients are so small that they are not visible in the numerical results of Fig. 2.4.3. Here we estimate the ADMRO effect in the lateral transport coefficients. Strictly speaking, the lateral transport coefficient, σ_{xx} also contains $[\sigma_{xx}]_0 \approx [\sigma_{zz}]_0 \tan^2\theta$, where $[\sigma_{xx}]_0$ is the conductivity due to the electron drift in high field limit. It can be seen by rotatiting the principal axes of the conductivity tensor components. We define u- and w- axes as shown in Fig 2.5.2-(a), where the u-axis is in the direction of magnetic field and the w-axis is perpendicular to it in the z-x plane.

For a closed orbit, the electron drift in the w- and y-direction

vanishes[5] because

$$\begin{aligned}\int_0^{2\pi} v_w(\varphi)d\varphi &= \oint v_\perp \cos\zeta \frac{\hbar}{m^*}\frac{dk_\parallel}{v_\perp} \\ &= \frac{\hbar}{m^*}\int dk_y \\ &= 0.\end{aligned} \tag{2.5.16}$$

Here, ζ is the angle defined in Fig.2.5.2-(b). Non-vanishing electron drift occurs only in the direction of magnetic field(u-direction). Thus it follows from eq.(2.5.3) that the conductivity components arising from electron drift vanish except for σ_{ww}.

We can determine $[\sigma_{xx}]_0$ by transformation of the principal axes,

$$\begin{pmatrix}\sigma_{xx} & \sigma_{xz}\\ \sigma_{zx} & \sigma_{zz}\end{pmatrix} = \begin{pmatrix}\cos\theta & \sin\theta\\ -\sin\theta & \cos\theta\end{pmatrix}\begin{pmatrix}\sigma_{ww} & \sigma_{wu}\\ \sigma_{uw} & \sigma_{uu}\end{pmatrix}\begin{pmatrix}\cos\theta & -\sin\theta\\ \sin\theta & \cos\theta\end{pmatrix}. \tag{2.5.17}$$

Since only σ_{ww} contains the conductivity due to the electron drift, we obtain

$$\begin{aligned}[\sigma_{xx}]_0 &= [\sigma_{zz}]_0 \tan^2\theta \\ &= \tan^2\theta\sigma^0_{zz}J_0^2(ak_F\tan\theta).\end{aligned} \tag{2.5.18}$$

The lateral conductivity components for $t/E_F \ll 1$ can be approximated by the pure two-dimensional conductivity (*i.e.* $t/E = 0$),

$$\sigma_{xx} = \frac{e^2n_e\tau}{m}\frac{(\frac{1}{\omega\tau})^2}{1+(\frac{1}{\omega\tau})^2},\ \sigma_{xy} = -\frac{e^2n_e\tau}{m}\frac{\frac{1}{\omega\tau}}{1+(\frac{1}{\omega\tau})^2}, \tag{2.5.19}$$

$$\sigma_{yy} = \sigma_{xx}, \qquad \sigma_{yx} = -\sigma_{xy},$$

where $\omega\tau = \omega_0\tau\cos\theta$. The most important correction is the $[\sigma_{xx}]_0$. Since $t/E_F \ll 1$, $\sigma_{xx} \gg [\sigma_{xx}]_0$ around $\omega\tau \sim 1$, thus ADMRO effect is small (negligible), as seen in Sec. 2.4. For a sufficiently large magnetic field, on the other hand, it becomes increasingly important because $\sigma_{xx} \sim [\sigma_{xx}]_0$ since two-dimensional conductivity component in σ_{xx} given by eq.(2.5.19) vanishes. On the other hand, the SdH oscillations will become prominent at the same field range and may mask the ADMRO effect. By contrast, the ADMRO effect is already manifest in ρ_{zz} for $\omega_0\tau \sim 1$ so that ρ_{zz} have the advantage in the observation of the large ADMRO effect.

2.6 Summary and Concluding Remarks

We have made semiclassical calculations of the conductivity tensor for a model quasi-two-dimensional system by use of the Shockley tube integral formula. The calculated resistivity ρ_{zz} exhibits angular dependent oscillations reminiscent of those recently found in the BEDT-TTF salts. The physical origin of the angular dependent oscillation lies in the distinct asymptotic behavior of the high field magnetoresistance (divergence *vs.* saturation) depending on the field angle relative to the corrugated Fermi surface. Since this is essentially a semiclassical effect, the ADMRO effect can be observed even when no SdH quantum oscillations are visible, in agreement with Kajita *et al.*'s observation. Similar phenomena should be observable in other quasi-two-dimensional conductors, provided that the shape of the Fermi surface is a weakly corrugated cylinder.

REFERENCES

1) K.Kajita, Y.Nishio, T.Takahashi, W.Sasaki, R.Kato, H.Kobayashi, A.Kobayashi and Y.Iye: Solid State Commun., 70(1989)1189.
2) M.V.Kartsovnik, P.A.Kononovich, V.N.Laukhin and I.F.Shchegolev: Sov. Phys.
JETP Lett., 48(1988)541.
3) K.Yamaji: J.Phys. Soc. Jpn., 58(1989) 1520.
4) K.Kajita, Y.Nishio, T.Takahashi, W.Sasaki, R.Kato, H.Kobayashi and A.Kobayashi: Solid State Commun., 70(1989)1181.
5) J.M.Ziman :"Principles of Theory of Solids", (Cambridge University Press, Cambridge, 1972), 2nd ed., p.301.

Chapter 3

The ADMRO Effect in GaAs/AlGaAs Superlattice

Magnetotransport studies of GaAs/Al_xGa_{1-x}As superlattice having a tailored Fermi surface of a weakly corrugated cylindrical shape have revealed an angular dependent magnetoresistance oscillation effect similar to the one found in quasi-two-dimensional organic conductors. The present observation provides evidence that the effect should commonly occur in a general class of nearly two-dimensional electron systems. Transport behavior has been studied both in the vertical and the lateral direction of the superlattice, and is discussed in the light of our semiclassical calculation described in the previous Chapter.

3.1 Introduction

Ever since the original proposal by Esaki and Tsu[1], world-wide intensive efforts have been paid to the development of science and technology of artificial semiconductor superlattices. With the advent of molecular beam epitaxy (MBE), superlattice technology has made a great progress, and it is now established that to a great extent semiconductor systems with tailored electronic structure can be fabricated. One of the early demonstrations of artificial electronic band structure was made by Chang *et al.*[2] who observed the SdH effect in GaAs/Al_xGa_{1-x}As superlattices and discussed in terms of minigap and miniband formation associated with the superlattice periodicity.

In a semiconductor superlattice, periodicity along the stacking direction (z-direction) leads to formation of one-dimensional subbands and subgaps in the energy dispersion along the k_z-direction. If the Fermi level resides within a 1D subband, the Fermi surface is closed within the first Brillouin zone. In this case the electronic structure is essentially three-dimensional, albeit anisotropic. If, on the other hand, it falls in a 1D subgap, the Fermi surface becomes a corrugated cylinder extended along the k_z-direction and the system is more two-dimensional in character. Thus, one can tailor the topology of the Fermi surface by appropriate choice of parameters, such as superlattice periodicity, barrier height, and doping level[9].

In this work, we tailor a Fermi surface appropriate for occurrence of the ADMRO effect by fabricating GaAs/$Al_xGa_{1-x}As$ superlattices and study their magnetotransport behavior as a function of field angle. The primary purpose of the present study using semiconductor superlattices is, of course, an experimental verification of the occurrence of the ADMRO effect in a system other than the organic conductors. Once it is achieved, superlattice system has a number of merits. Namely, we can study the effect with a tailored Fermi surface. Furthermore, different resistivity components can be unambiguously measured by fabricating devices of appropriate geometry. The latter point is related with the discrepancy mentioned in the previous Chapter between the experimental observation in organic conductors and our results.

This Chapter is organized as follows. In the next section the experimental methods including the superlattice design and fabrication is described. Experimental results are presented and discussed in Section 3.3, and Section 3.4 gives concluding remarks.

3.2 Experimental

3.2.1 Design and Fabrication of Superlattice Samples

In order to optimize the experimental condition for observation of the ADMRO effect in a GaAs/ $Al_xGa_{1-x}As$ superlattice, the following factors have to be taken into consideration:

(i) The shape of the Fermi surface should be a weakly corrugated cylinder. The Fermi surface can be designed by adjusting such parameters as the superlattice period, the alloy composition x, and the doping concentration.

(ii) The corrugation should be weak, which requires the interlayer transfer matrix element to be small. However, it should not be smaller than the energy broadening by impurity scattering.

(iii) High carrier density is favored in order to attain the a semiclassical situation at high fields. It has to be compromised, however, with decreasing carrier mobility (and hence $\omega\tau$) with increased doping.

(iv) In order to measure the vertical transport, the number of layers should be made as large as possible within the limit of practical

Device I.D.	*Type*	E_F *[meV]*	n_e $[cm^{-3}]$
L_1	ρ_{xx}, ρ_{xy}	29	5×10^{17}
V_1	ρ_{zz}	29	5×10^{17}
L_2	ρ_{xx}, ρ_{xy}	45	7.5×10^{17}
V_2	ρ_{zz}	45	7.5×10^{17}

Table 3.2.1 Designed device parameters. E_F: Fermi energy, n_e:Designed carrier density.

growth conditions.

With the above considerations, the following parameter values have been chosen. The thickness of the GaAs layer is 100 Å. The $Al_xGa_{1-x}As$ layer is 60 Å thick with the alloy composition, $x = 0.15$. With this superlattice structure, the lowest subband width is 6 meV and the first minigap width is 50 meV. To realize a corrugated cylindrical Fermi surface, the Fermi energy must lie in the first minigap. The structure and the parameter values of superlattice devices are summarized in Table 3.2.

Samples of GaAs/ $Al_xGa_{1-x}As$ superlattice used in the present study were grown by a molecular beam epitaxy (MBE) method. Two types of devices (vertical and lateral transport) for the above superlattice structure were grown under the same growth condition.

The device I.D.'s have the following meaning. The symbol L(V) means that the device is fabricated into a geometry for lateral (vertical) transport measurement. Devices with the same suffix (like L_1 and V_1) are the cut out of the samples grown under the same condition.

Devices V_1 and V_2 for the vertical transport (ρ_{zz}) were prepared by successively growing on a ⟨100⟩n^+-GaAs substrate, a 500 Å thick of n^+-GaAs buffer layer, 100 units of GaAs (100 Å) /$Al_xGa_{1-x}As$ (60 Å) superlattice (total thickness 16,000 Å), and finally a 5000 Å of n^+-GaAs cap layer. Si donors were doped only in the $Al_xGa_{1-x}As$ layers to attain a high mobility. Typical growth rate was $\sim$ 2Å/sec.

Devices L_1,L_2 for measurements of lateral transport (ρ_{xx} and ρ_{xy}) were prepared by successively growing on a semi-insulating ⟨100⟩GaAs substrate, a 500 Å thick GaAs buffer, 100 units of GaAs (100 Å)/

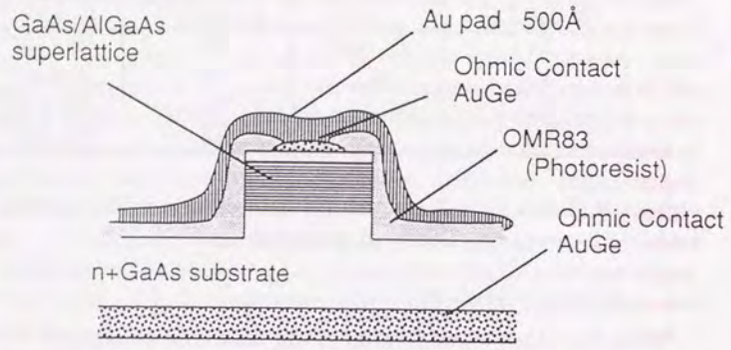

Fig 3.2.1 Schematic diagram of the device structure of the vertical transport sample.

$Al_xGa_{1-x}As$ (60 Å), 100 Å thick of $Al_xGa_{1-x}As$, n^+-$Al_xGa_{1-x}As$ and GaAs.

We have examined the superlattice periodicity by X-ray diffraction. The period of the grown superlattices turned out to be 130Å, about 19% smaller than the designed value.

The device structure for the vertical transport measurement was depicted in Fig. 3.2.1. The fabrication was done by the following process. First AuGe alloy was deposited ($\sim 2000\mathring{A}$ thick) on both side of the substrate and patterned by a usual photolithography technique to form Ohmic contacts. The alloying was done at about 400°C for 1 min in Ar. The superlattice samples were patterned by wet etching in $1H_2O_2 : 1H_3PO_4 : 8H_2O$ solution. A series of Devices with different lateral dimensions ($50 \times 50, 100 \times 100, 200, \times 200\mu m^2$ *etc.*) were prepared, in order to confirm that the measured conductance scaled with the cross-sectional area. Insulating layer was formed with a photoresist OMR-83 ($\sim 1\mu$m thick), and then Au ($\sim 500\mathring{A}$ thick) was deposited to spread the top electrode.

Devices for the lateral transport measurement was patterned in

a standard Hall bar geometry by wet etching. The channel of the Hall bar is 50 μm wide and the distance between the voltage probe was 200 μm. Ohmic contacts were achieved with AuGe alloy.

3.2.2 Magnetotransport Measurements

The magnetotransport measurements were carried out in a 9 T superconducting solenoid using the rotating sample holder. Transport measurements were done using a direct current, typically 100 μA. Both ρ_{xx} and ρ_{xy} were simultaneously measured for devices for lateral transport in a standard way. Because of its structure, resistance measurements of vertical transport device were done by a two-probe method. By a method described in the next section, we were able to extract the vertical resistance of the superlattice part from the measured two-probe resistance. The angle of magnetic field is monitored by a set of Hall sensors on the sample mounting stage. Temperature was monitored by a carbon glass thermometer. The temperature control was done by use of an analog P.I.D. temperature controller.

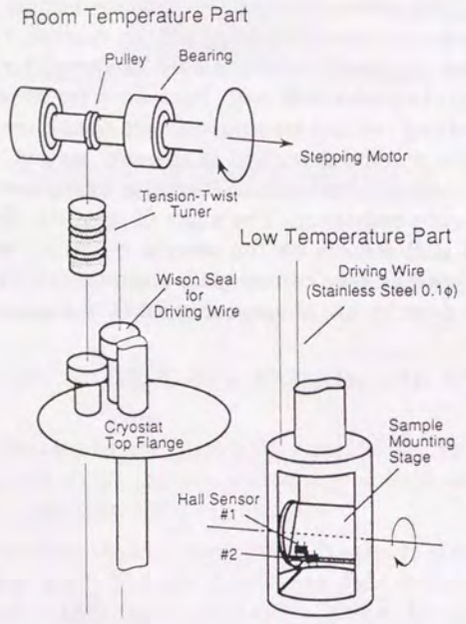

Fig. 3.2.2 Schematic diagram of rotating sample holder.

3.2.3 Rotating Sample Holder

Fig.3.2.2 shows the structure of the rotating sample holder. The sample mounting stage is rotated by a set of pulley and wire. The rotating action is delivered from the top of the cryostat by a thin wire to the sample mounting stage. The tension and twists of the driving wire are tuned by the apparatus inserted in the wire loop. The action of the driving wire is precisely controlled by a stepping motor (minimum step $\sim 0.03°$) on top of the cryostat. Two Hall sensors are mounted on the rotating stage so that they monitor the vertical and horizontal components of magnetic field. This type of rotating mechanism enables us to sweep the field angle more smoothly than those using gear assemblies, and to investigate subtle features in angular dependence.

3.3 Results and Discussion

3.3.1. Sample Characterization

The electron densities of the present samples are estimated from the Hall coefficient and the SdH effect of Devices L_1 and L_2 for lateral transport measurement at $T = 4.2$ K. The obtained parameters are summarized in Table 3.3.3. These values are obtained by assuming a cylindrical Fermi surfaces. The analysis of the angular dependence of the SdH period indicates that the Fermi surface is a weakly corrugated cylinder, as designed. The Devices V_1,V_2 for the vertical transport measurement also show the SdH oscillations at low temperatures. The SdH periods for Devices V_i and L_i agree with each other, as they should.

Device I.D.	$n_H[cm^{-3}]$	n_{SdH} $[cm^{-3}]$	μ $[cm^2/Vsec]$
L_1	6.5×10^{17}	6.8×10^{17}	2040
L_2	8.9×10^{17}	9.9×10^{17}	2960

Table 3.3.3
Carrier density and mobility of grown superlattice samples. n_H:Carrier density determined by Hall effect at T=4.2K, n_{SdH}: Carrier density determined by the SdH effect at T=4.2K, μ: Electron mobility.

3.3.2 Vertical Transport

Figure 3.3.1 shows the angular dependence of the resistance of the Device V_1 at T = 30 K under different magnetic fields up to 9 T. With increasing field intensity, resistance peaks at $\theta^{(1)}_{max} \sim 39°$ and at $\theta^{(2)}_{max} \sim 62°$ become manifest. It should be noted that the field angle of the peak structure does not depend on the field intensity. This fact rules out the usual SdH effect or magnetophonon effect as the origin of these features.

The reason why the above measurement is done at T = 30 K is because the SdH oscillations becomes increasingly dominant at lower temperatures. Figure 3.3.2 shows the magnetic field dependence of resistance for different field angles at T = 30 K. A weak SdH oscillation is seen at $\theta = 0°$ (Trace a) even at this high temperature, but the amplitude of the SdH oscillations rapidly diminishes with tilt angle. It is emphasized that at $\theta \sim 39°$ (Trace b) where the most prominent peak structure occurs in the angular traces, the field dependence shows no structure.Thus, the structures in the $\rho_{zz}(\theta)$ traces shown in Fig. 3.3.1 have the characteristics of the ADMRO in common with that in the organic conductors.

Figure 3.3.3 shows the angular traces of resistance at different temperatures from 4.2 K to 145 K. At higher temperatures ($T >$ 100 K), only the resistance peak at $\theta = \theta^{(1)}_{max}$ is visible. The second peak at $\theta = \theta^{(2)}_{max}$ becomes clearly discernible at intermediate tem-

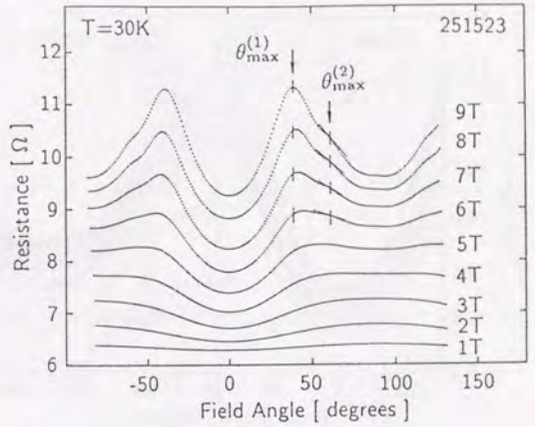

Fig. 3.3.1 The angular dependence of the vertical resistance, ρ_{zz}, of Device V_1 at T = 30 K for different field intensities.

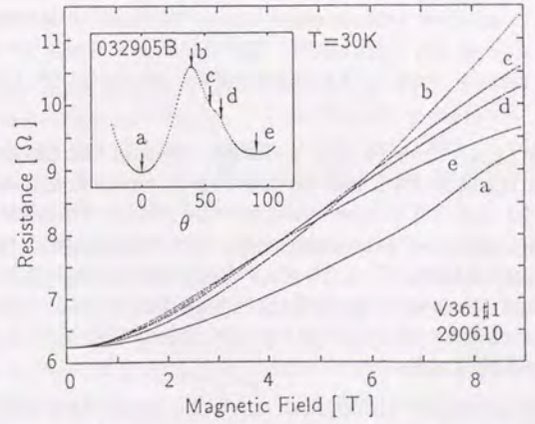

Fig. 3.3.2 Magnetic field dependence of the vertical resistance, ρ_{zz}, of Device V_1 at T = 30 K for different field angles. The selected field angles (a to e) are indicated in the inset.

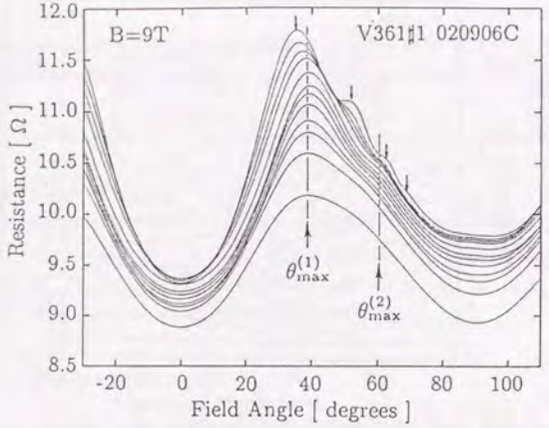

Fig. 3.3.3 The angular dependence of the vertical resistance, ρ_{zz}, of Device V_1 at different temperatures. From top to bottom, $T = 4.2$K, 10.3K, 15.3K, 19.6K, 30K, 38K, 44K, 53K, 67K, 83K, 110K, and 145K. The peaks in the low temperature traces marked by arrows are due to the SdH effect. The ADMRO peaks are most clearly seen in the intermediate temperature range.

perature range (100 K $> T >$ 15 K). This is the temperature range in which the ADMRO can be most clearly observed, and the data in Figs. 3.3.1 and 3.3.2 were taken in this range. Note that peak angles are independent of temperature in this temperature range. At still lower temperatures ($T <$ 15 K), other peaks (marked by arrows) due to the SdH effect emerge and grow with decreasing temperature. The positions of the two ADMRO peaks apparently shift by interference with the SdH peaks.

It is necessary to confirm that the observed phenomenon is intrinsic to the superlattice part of Device V_1, since the measured two-probe resistance is a series sum of the resistances of the superlattice, the n^+-GaAs substrate and the n^+-GaAs cap layer, and the contact resistances. For this purpose, we prepared three types of devices illus-

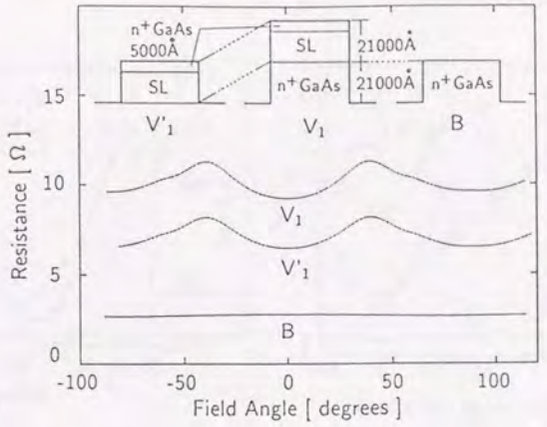

Fig. 3.3.4 Comparison of the angular dependence of ρ_{zz} for three devices (Devices V_1, V'_1 and B) with structures illustrated in the inset. The resistance behavior is consistent with the series sum of the resistances of different layers.

trated in the inset of Fig. 3.3.4. The middle figure shows the vertical structure of Device V_1. Device V'_1 on the left is identical with Device V_1 except that the etching process is stopped right at the bottom of the superlattice part. Device B on the right is a mesa of bulk n^+-GaAs which corresponds to the lower half of the Device V_1.

The main panel of Fig. 3.3.4 shows the angular dependence of magnetoresistance of the three devices at $T = 30$ K and $B = 9$ T. The angular traces of resistance of Devices V_1 and V'_1 show the identical peak structure. They differ by an amount corresponding to the resistance of Device B, which depends very weakly and monotonically on the magnetic field direction. The contact resistance and the resistance of the unetched n^+-GaAs substrate part are negligible in this scale. Thus, it is firmly established that the peak structures seen in Devices V_1 and V'_1 are intrinsic to the superlattice part.

Next we turn to the carrier density dependence. The left panel

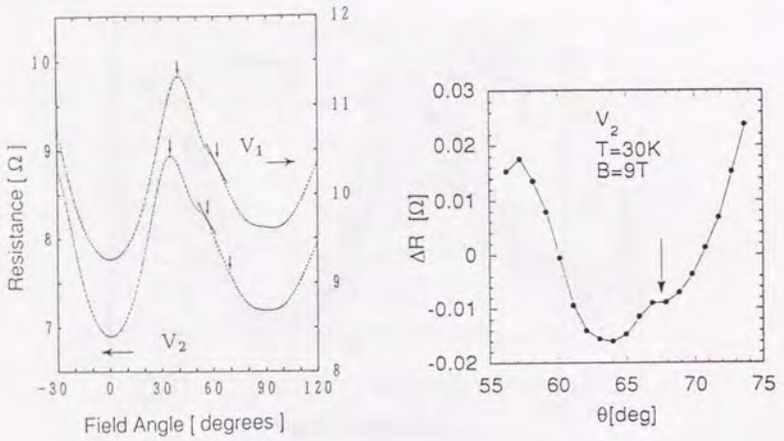

Fig. 3.3.5 Left:Angular dependence of ρ_{zz} of Device V_2 at B=9T, T = 30K. Data for Device V_1 are also plotted for comparison. Right: Enhanced plot of $\rho_{zz}(\theta)$ of Device V_2.

of Fig.3.3.5 shows the angular dependence of magnetoresistance for Device V_2 at T = 30K,B = 9T. The result for Device V_1 is also plotted in the same figure for comparison. It is seen that the resistance curve for Device V_2 is approximately the same as Device V_1 although peaks are shifted to the lower angles. The peaks in Device V_2 occur at $\theta = 34°$, 57° and 68°. The right panel of Fig.3.3.5 shows the enhanced plot of the angular dependence of resistance around the third peak. The deviation from linearity is plotted. The third peak $\theta = 68°$ is visible in this plot.

In contrast to the case of organic conductors where the ADMRO peaks up to $n \sim 8$ have been observed, only a few peaks are seen in the present case. According to our calculation[6] (Fig.2.4.1), the ADMRO starts to develop above $\omega\tau \sim 1$. From the basal-plane Hall mobility at this temperature, we estimate $\omega\tau \sim 1.8$ at B = 9 T for $\theta = 0°$, which is the reason why only two or three peaks are observed in V_1. In Device V_2 we could observe three peaks since it has a larger

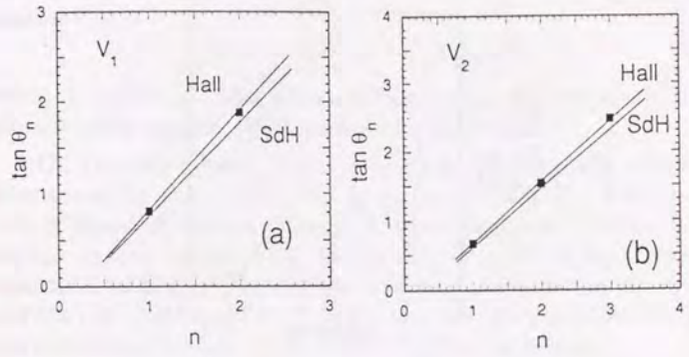

Fig. 3.3.6 Comparison of the observed peak angles of the ADMRO in (a) Device V_1 and (b) Device V_2, with the peak condition (eq.(2.5.13)). Solid points are observed peak data at T = 30K. Lines are the eq.(2.5.13)with the carrier density determined by the Hall effect and the SdH effect.

electron mobility than Device V_1.

Another possible origin of the rapid decrease of the ADMRO at higher angles may be sought in the fact that the deviation from a weak corrugation condition tends to smear the ADMRO effect more effectively at higher angles.

Next we compare the observed peak angles with eq.(2.5.13). Fig. 3.3.6-(a) and (b) show the plot of the peak angles $\tan\theta_n$ against the peak index n. The $\tan\theta$ values obtained by eq.(2.5.13) using the superlattice parameters are also plotted for comparison. The observed peaks for both Devices V_1 and V_2 exhibit fairly good agreement with eq.(2.5.13).

The peak angles of V_2 shifts to lower angles because Device V_2 has larger k_F since carrier density for V_2 is larger than V_1. As seen in eq.(2.5.13) larger k_F cause a small θ_n for the same a. The angle

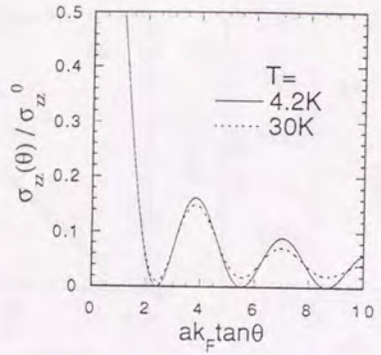

Fig. 3.3.7 Numerically calculated angular dependence of σ_{zz} in the high field limit for different temperatures. Here, $E_F = 350$K.

for the first peaks gives the relation

$$\frac{\tan\theta_{(V1)}}{\tan\theta_{(V2)}} = \frac{k_{F(V2)}}{k_{F(V1)}} = 1.21, \tag{3.3.1}$$

which fairly agrees with the same value obtained from carrier density,

$$\frac{k_{F(V2)}}{k_{F(V1)}} \approx \sqrt{\frac{n_H(V2)}{n_H(V1)}} = 1.17, \tag{3.3.2}$$

$$\sqrt{\frac{n_{SdH}(V2)}{n_{SdH}(V1)}} = 1.20. \tag{3.3.3}$$

We were able to observe the ADMRO effect by conducting the experiment in an intermediate temperature range so as to avoid intervention of the SdH oscillations. This fact indicates that the temperature-induced smearing acts differently on the ADMRO effect and on the SdH effect.

The amplitude of the SdH effect for $\omega\tau \gg 1$ is determined by $\hbar\omega$ and k_BT. The SdH amplitude is approximately given by the relation[10],

$$(SdH\ amplitude) \propto X/\sinh X, \tag{3.3.4}$$

where $X = 2\pi^2 k_BT/\hbar\omega$. The condition for the occurrence of the SdH effect is often roughly approximated by $\hbar\omega > k_BT$.

On the other hand, the temperature effect on the ADMRO is determined by the $-(\partial f^0/\partial E)$ factor in eq.(2.2.12). The electrons with different E (hence different k) contribute to σ with different angular period (eq.(2.5.13)). In the case of $\omega\tau \gg 1$, k_BT should be compared with E_F. The distribution Δk is approximately given by $(\Delta k/k_F) \sim (1/2)(k_BT/E_F)$. We formulate the condition for occurrence of the n-th peak of the ADMRO effect as follows:

$$n\left(\frac{\pi}{a\left(k_F - \frac{\Delta k}{2}\right)} - \frac{\pi}{a\left(k_F + \frac{\Delta k}{2}\right)}\right) < \frac{1}{2}\left(\frac{\pi}{ak_F}\right). \tag{3.3.5}$$

This is the condition where the phase difference of the ADMRO effect between $k \sim k_F - (\Delta k/2)$ and $k \sim k_F + (\Delta k/2)$ states becomes π. In terms of k_BT and E_F, the above condition can be written as

$$n \cdot \frac{k_BT}{E_F} < 1. \tag{3.3.6}$$

We note that for large n, the temperature effect becomes significant. In the case of usual metals, $E_F \gg k_BT$ (and usually $E_F \gg \hbar\omega$) , so that the ADMRO effect survives much higher temperatures than the SdH effect when $\omega\tau > 1$.

In the present case ($E_F \sim 350$K), we have observed the ADMRO effect at $T = 30$K where the SdH effect is diminished. We estimate the amplitude of the both effects. First we note that the carrier density and the zero-field resistance does not exhibit significant change between $T = 4.2$K and 30K so that the value of $\omega\tau$ does not change. Fig. 3.3.7 shows the numerical result of $\sigma_{zz}(\theta)$ in the high field limit for $T = 4.2$K and $T = 30$K. We can see the temperature induced broadening of the oscillation for $T = 30$K, but the ADMRO amplitude is still comparable to that for $T = 4.2$K. On the other hand, the SdH

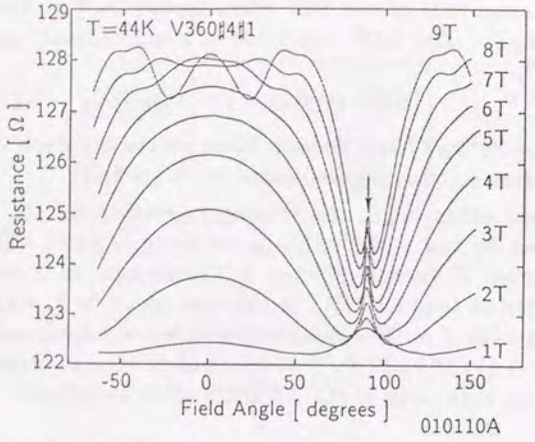

Fig. 3.3.8. The angular dependence of the lateral resistance of Device L_1 at $T = 44$ K for different field intensities. The traces in this figure were obtained by rotating the magnetic field from the direction normal to the layer to the direction of the current. The same result was obtained when the field was rotated within the plane perpendicular to the current direction.

amplitude obtained by eq.(3.3.4) with $B = 9$T, $T = 30$K, $\theta = 60°$ is about 1% of that at $T = 4.2$K so that it is negligible at $T = 30$K. Thus we can observe only the ADMRO effect by suppressing the SdH effect around T$\sim$ 30K.

Since the ADMRO effect is attributed to the semiclassical behavior of electrons in magnetic field, it can survive up to much higher temperatures than the quantum magneto-oscillation effect. Quantitative discussions of the temperature dependence of both the ADMRO effect and the SdH effect require a quantum mechanical calculation of the conductivity tensor components.

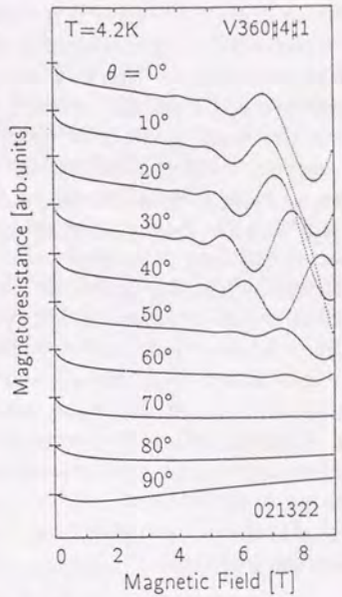

Fig.3.3.9 The field dependence of the lateral resistance of Device L_1 at $T = 4.2$ K for different field angles.

3.3.3 Lateral Transport

Figure 3.3.8 shows the angular dependence of ρ_{xx} of Device L_1 at different field intensities. Although the measurement was done at $T = 44$ K to suppress the amplitude of the SdH oscillations, the main features in the angular dependence are due to the SdH effect. Apart from the features due to the SdH effect and a cusp-like structure at $\theta = 90°$, the angular dependence of ρ_{xx} is featureless. In particular, it is noted that there is no peak structure at around $\theta = 39°$ which corresponds to the first peak of ρ_{zz} in Device V_1. The absence of the ADMRO in ρ_{xx} is in agreement with our calculation[6]. The cusp-like structure at $\theta = 90°$ is attributed to the negative magnetoresistance due to localization effect, which will be discussed in Appendix B.

Figure 3.3.9 shows the magnetoresistance, $\rho_{xx}(B)$, of Device L_1 at different angles at $T = 4.2$K. As θ is increased, the period of the SdH oscillations decreases and the amplitude diminishes, as expected for a cylindrical Fermi surface. The SdH amplitude, however, does not appear to decrease monotonically with θ, although it is difficult to judge based on the small number of observed oscillations. It is noted that the amplitude diminishes rapidly between $\theta = 40°$ and $50°$, and appears to take a local maximum between $\theta \sim 20°$ and $40°$. The angle at which the SdH amplitude becomes maximum is in the neighborhood of the first peak angle of ρ_{zz} in Device V_1. This is consistent with the prediction based on Yamaji's model, because all the Fermi surface cross-sections coincide at this angle. Because its physical origin lies in a coincidental enhancement of the Fermi surface density of state effect, this SdH amplitude modulation is expected to occur regardless of the current direction, which is in contrast with the semiclassical ADMRO effect. It has to be added, however, that the observed amplitude change could possibly arise from beating of the SdH oscillations with different periods, so that it is difficult to make any definite statement about the amplitude based on the small number of oscillations observed.

3.4 Conclusion

We have succeeded in the experimentally demonstrating the angular dependent magnetoresistance oscillation effect in GaAs/$Al_xGa_{1-x}As$ superlattices. The present result provides an evidence that the ADMRO effect can occur in a general class of nearly two-dimensional electron systems. We have observed a qualitative difference in the angular dependent magnetoresistance between lateral and vertical transport. Namely, as we proposed in the previous Chapter, the ADMRO effect is manifest only in ρ_{zz}. On the other hand, the amplitude of the SdH oscillations of ρ_{xx} appears to show an angular dependence as predicted by Yamaji's theory[5]. The physical origin is common to the both effects, and lies in the occurrence of special situation of the electron orbits for particular set of field angles specified by eq.(2.5.13).

For the study of the ADMRO effect, the semiconductor superlattice system offers a large degree of freedom for Fermi surface tailoring by adjusting the superlattice periodicity and doping. On the other

hand, the achievable carrier density is rather limited and at the sacrifice of carrier mobility. As mentioned in the previous section, this makes a quantitative discussion of the angular dependence of the SdH amplitude difficult. It would be interesting to study the ADMRO effect in systems with higher electron densities (larger Fermi surfaces). Artificial metallic superlattices and graphite intercalation compounds are possible candidates for such studies.

We have tried to observe the ADMRO effect in graphite intercalation compounds $C_{24}SbCl_5$ and in Si/Ag metallic multilayers.

In the case of graphite intercalation compounds, although we observed a subtle hump-like structure in the angular dependence of magnetoresistance around $\theta \sim 75°$,the feature was too weak to make any definite statement.

In the experiments on the artificial metallic superlattices, we have encountered difficulties in the sample fabrication. First, the epitaxial growth of artificially structured superlattice is difficult to achieve. Secondly, the vertical resistance of metallic multilayer film is so small that films have to be patterned in a small enough dimension by use of a photolithograph technique. We have confronted troubles in the etching of the multilayer film.

These attempts are so far unsuccessful and are left for future challenge.

References

1) L.Esaki and R.Tsu: IBM J. Res. Develop., **14** (1970) 61.
2) L.L.Chang, H.Sakaki, C.A.Chang, and L.Esaki: Phys. Rev. Lett., **38** (1977) 1489.
3) K.Kajita, Y.Nishio, T.Takahashi, W.Sasaki, R.Kato, H.Kobayashi, A.Kobayashi, and Y.Iye: Solid State Commun., **70** (1989) 1189.
4) M. V. Kartsovnik, P. A. Kononovich, V. N. Laukhin and I. F. Schegolev: Sov. Phys. JETP Lett., 48 (1988) 541; V. N. Laukhin, M. V. Kartsovnik, S. I. Pesotiskii, I. F. Schegolev, and P. A. Kononovich: *"Physics and Chemistry of Organic Superconductors "* , *eds.* G. Saito and S. Kagoshima, (Springer-Verlag, Heidelberg, 1990) p.186.
5) K.Yamaji: J. Phys. Soc. Jpn., **58** (1989) 1520.
6) R.Yagi, Y.Iye, T.Osada, and S.Kagoshima: J. Phys. Soc. Jpn., **59** (1990) 3069.
7) J.M.Ziman: *"Principles of the Theory of Solids"*, (Cambridge University Press, Cambridge, 1982) 2nd ed. p.301.
8) T.Osada, R.Yagi, S.Kagoshima, N.Miura, M.Oshima, and G.Saito: *"Physics and Chemistry of Organic Superconductors"*, *eds.* G. Saito and S. Kagoshima, (Springer-Verlag, Heidelberg, 1990) p.220.
9) J.Yoshino, H.Sakaki, and T.Furuta: *Proc. 17th Int. Conf. Phys. Semicond., San Francisco, 1984*, (Springer 1985) p.159.
10) L.M.Loth, and P.N.Argyres: *"Semiconductors and Semimetals"* vol.1, (Academic Press 1966).

Chapter 4

The ADMRO Effect of Cylindrical Fermi Surfaces with Different Corrugation Symmetries

We have studied the angular dependence of magnetoresistance for some cylindrical Fermi surfaces with different corrugation symmetries. It is shown that angular dependent magnetoresistance oscillation (ADMRO) exhibits a wide variety of behavior depending on the corrugation symmetry. In particular, some types of corrugation symmetry yield an inverted peak and valley structure. We discuss the possible relevance of the present result to the experimentally observed peak inversion of the ADMRO in a certain class of organic conductors.

4.1 Introduction

As seen in Chapters 1-3, the standard ADMRO effect has been successfully explained by a cylindrical Fermi surfaces. In the meanwhile it has been recognized that some compounds in the same family such as (BEDT-TTF)$_2$KHg(SCN)$_4$[6] and (BEDT-TTF)$_2$TlHg(SCN)$_4$[7] exhibit an anomalous ADMRO effect.

Figure 4.1.1 shows the angular dependence of magnetoresistance in (BEDT-TTF)$_2$ KHg(SCN)$_4$[6]. As seen in the figure, the ADMRO effect exhibit an inverted peak as compared with the standard ADMRO effect in that $\theta = 0°$ is the peak angle while it is a valley in the standard ADMRO effect.

The origin of the "inverted" ADMRO is currently unknown. We address to this issue by investigating the ADMRO effect of a few cylindrical Fermi surfaces with different types of corrugation symmetries. Since the ADMRO effect originates from the Fermi surface corrugation, a slight change of the corrugation pattern may result in a significant difference in ADMRO phenomenon. We investigate the ADMRO effect for four model Fermi surfaces with different corrugation symmetries, within the framework of the Boltzmann transport theory.

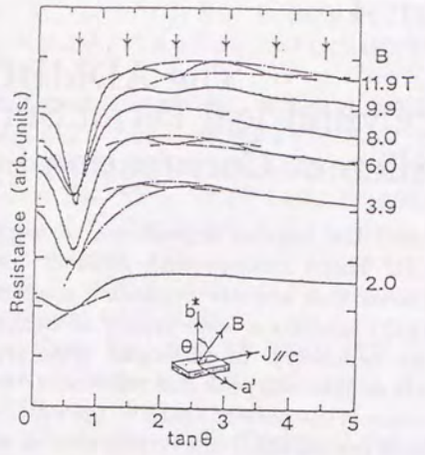

Fig. 4.1.1 Angular dependence of magnetoresistance of $(BEDT\text{-}TTF)_2KHg(SCN)_4$. $T = 4.2K$. From top to bottom, $B = 12, 10, 8, 6, 4, 2T$. (After Osada and Yagi *et al.* [6])

This Chapter is organized as follows. In the next section, we define the model Fermi surfaces with different corrugation patterns. In Section 4.3, we present the calculated results and discuss their possible relevance to the experimental findings.

4.2 Model

We consider four model Fermi surfaces with different corrugation symmetries as shown in Fig. 4.2.1. These Fermi surfaces correspond to the following energy dispersion relations arising from different k_x,k_y-dependences of the transfer integral.

$$\text{[A]} \qquad E = \frac{\hbar^2}{2m}\left(k_x^2 + k_y^2\right) - 2t\cos\left(ak_z\right), \tag{4.2.1}$$

$$\text{[B]} \qquad E = \frac{\hbar^2}{2m}\left(k_x^2 + k_y^2\right) - 2t\cos\left(ak_z\right)\frac{k_x}{\sqrt{k_x^2 + k_y^2}} \tag{4.2.2}$$

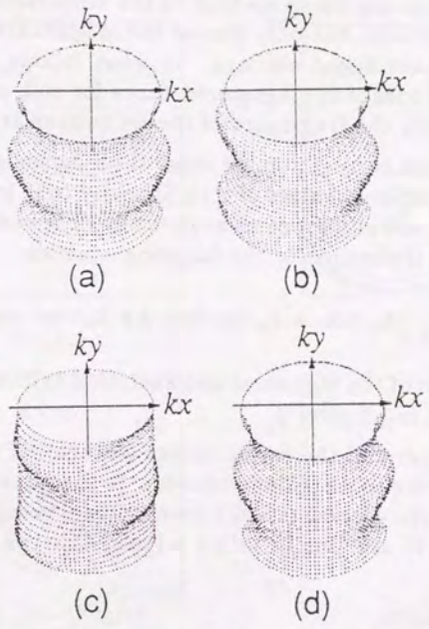

Fig 4.2.1 Schematic diagram of model Fermi surfaces with different corrugation symmetries: (a)s-type,(b)p-type,(c)d_{xy}-type,(d)d_{xx}-type corrugation.

[C] $$E = \frac{\hbar^2}{2m}\left(k_x^2 + k_y^2\right) - 2t\cos\left(ak_z\right)\frac{k_x k_y}{k_x^2 + k_y^2}, \quad (4.2.3)$$

[D] $$E = \frac{\hbar^2}{2m}\left(k_x^2 + k_y^2\right) - 2t\cos\left(ak_z\right)\frac{k_x^2}{k_x^2 + k_y^2}. \quad (4.2.4)$$

We do not concern ourselves here to the microscopic origins of these energy dispersions, but only discuss the magnetotransport properties of the resultant Fermi surfaces. In what follows, we calculate the angular dependence of magnetoresistance for each of the model Fermi surfaces within the framework of the Boltzmann transport theory.

For a weak corrugation, we study the θ-dependence of magnetoresistance for different values of ϕ by Shockley tube integral (eq.(2.3.4)) numerically, and in some cases analytically. The variable k_0 in eq.(2.3.1) for this case is changed to the following equation:

$$k_0 = k_z + k_x \tan\theta\cos\phi + k_y \tan\theta\sin\phi. \quad (4.2.5)$$

The methods of the numerical and analytical calculation are the same as described in Chapter 2.

We simply call the Fermi surface corrugation given by eq.(4.2.1) s-type referring to its radial symmetry. In the same manner, the types of Fermi surface corrugation corresponding to eq.(4.2.2), eq.(4.2.3) and eq.(4.2.4) are simply called p-type, d_{xy}-type and d_{xx}-type, respectively.

4.3 Results and Discussion

As we have pointed out in Chapter 2, the angular dependent magnetoresistance oscillation in a weakly corrugated cylindrical Fermi surface occurs principally in the vertical transport. For this reason, we restrict ourselves to the vertical conductivity.

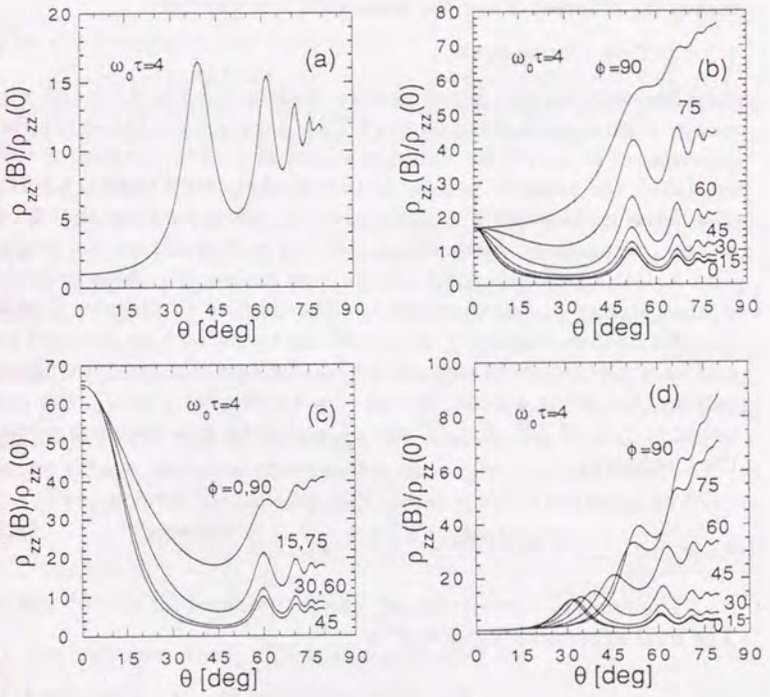

Fig. 4.3.1 Numerically calculated $\rho_{zz}(\theta)$ for different values of ϕ for (a)s-type, (b)p-type, (c)d_{xy}-type and (d)d_{xx}-type corrugation Fermi surface. The parameter values for these figures are $E_F/t = 100$,$mta^2/\hbar^2$=0.045.

4.3.1 s-Type Corrugation

The ADMRO effect for this Fermi surface is the standard ADMRO effect. We only comment on the ϕ-dependence. Figure 4.3.1-(a) shows a numerically obtained θ-dependence of magnetoresistance ($\rho_{zz}(\theta)$) for different values of ϕ. The parameter values for this figure are the same as Fig.2.4.1. As expected from the radial symmetry, the $\rho_{zz}(\theta)$ curves for different ϕ are the same with one another.

4.3.2 p-Type Corrugation

Next we consider the Fermi surface depicted in Fig 4.2.1-(b) whose energy dispersion is given by eq.(4.2.2). Figure 4.3.1-(b) shows the θ-dependence of $\rho_{zz}(\theta)$ for different values of ϕ. The parameter values are taken the same as before. It is seen that the ADMRO effect for this Fermi surface exhibits a considerable difference from that for the s-type corrugation. First, the $\rho_{zz}(\theta)$ curve depends on the angle ϕ. The ADMRO effect is most clearly seen at $\phi = 0°$. With increasing ϕ, the value of $\rho_{zz}(\theta)$ increases and the relative amplitude of oscillation diminishes. Secondly, the $\rho_{zz}(\theta)$ curves exhibit an inverted peak and valley structure as compared with the case of s-type corrugation, namely, $\theta = 0°$ is a peak instead of a valley. For $\phi = 0°$, the peaks occur at $\theta \sim 0°$,52°, 67°,73°,*etc.* These peak positions are given by the condition,

$$ak_F \tan\theta_n = \pi\left(n - \frac{3}{4}\right) \qquad n : \text{integer}. \tag{4.3.1}$$

The analytic formula for σ^p_{zz} can be obtained for $\phi = 0°$ and 90°. The final expression for $\phi = 0°$ is

$$\sigma^p_{zz}(\theta, \phi = 0°) = \sigma^0_{zz} \sum_{\nu=-\infty}^{\infty} \frac{1}{4} \frac{\left(J_{\nu-1}(ak_F \tan\theta) - J_{\nu+1}(ak_F \tan\theta)\right)^2}{1 + (\nu\omega_0\tau\cos\theta)^2}. \tag{4.3.2}$$

Here, σ^0_{zz} is given by eq.(2.5.15). The high field magnetoresistance is governed by the $\nu = 0$ term in the summation. The asymptotic form of σ^p_{zz} is given by

$$\sigma^p_{zz}(\theta, \phi = 0°) \approx \sigma^0_{zz} J_1^2(ak_F \tan\theta). \tag{4.3.3}$$

The peak position of $\rho_{zz}(\theta)$ for this case is given by the *zeros* of the first order Bessel function. For $ak_F \tan\theta \gg 1$ this condition is given by eq.(4.3.1), which however exhibits deviation for small $ak_F \tan\theta$.

The analytic formula for σ^p_{zz} for $\phi = 90°$ is given by

$$\sigma^p_{zz}(\theta, \phi = 90°) = \sigma^0_{zz} \sum_{\nu=-\infty}^{\infty} \frac{1}{4} \frac{\left(J_{\nu-1}(ak_F \tan\theta) + J_{\nu+1}(ak_F \tan\theta)\right)^2}{1 + (\nu\omega_0\tau\cos\theta)^2}. \tag{4.3.4}$$

The $\nu = 0$ terms in the summation, $(\sigma^0_{zz}/4)\left(J_1(ak_F \tan\theta) + J_{(-1)}(ak_F \tan\theta)\right)^2$ vanish since $J_{(-1)}(z) = -J_1(z)$. In the high field limit, σ^p_{zz} vanishes for all θ, thus the ADMRO effect becomes much smaller in magnitude at $\phi = 90°$.

4.3.3 d_{xy}-Type Corrugation

Next we consider the ADMRO effect for the Fermi surface illustrated in Fig.4.2.1-(c). The energy dispersion for this Fermi surface is given by eq.(4.2.3). Fig.4.3.1-(c) shows a numerically obtained $\rho_{zz}(\theta)$ for different values of ϕ. The largest ADMRO effect occurs at $\phi = 45°$ and the smallest at $\phi = 0°$ and 90°. The ADMRO effect for this Fermi surface has a four-fold symmetry in ϕ-rotation. The $\rho_{zz}(\theta)$ for $\phi = 45°$ has peaks at $\theta \approx 0°$,60°,70°,76°, *etc.* The first peak occurs at $\theta = 0°$ similarly to the case of the p-type corrugation, but the oscillations at larger θ have the same phase as for the s-type corrugation.

The analytic formula for σ^{dxy}_{zz} for $\phi = 45°$ is obtained as follows

$$\sigma^{dxy}_{zz}(\theta, \phi = 45°) = \sigma^0_{zz} \sum_{\nu=-\infty}^{\infty} \frac{1}{16} \frac{\left(J_{\nu-2}(ak_F \tan\theta) + J_{\nu+2}(ak_F \tan\theta)\right)^2}{1 + (\nu\omega_0\tau\cos\theta)^2}. \tag{4.3.5}$$

In the high field limit, σ^{dxy}_{zz} is approximated by

$$\sigma^{dxy}_{zz}(\theta, \phi = 45°) \approx \frac{\sigma^0_{zz}}{4} J_2^2(ak_F \tan\theta). \tag{4.3.6}$$

Thus, the peak angles θ_n of the ADMRO effect are given by the *zeros* of the second order Bessel function. The *zeros* for large $ak_F \tan\theta$ is given approximately by

$$ak_F \tan\theta_n = \left(n - \frac{1}{4}\right) \qquad n : \text{integer}, \tag{4.3.7}$$

which is the same as the s-type case.

For $\phi = 0°$ the final expression for σ_{zz}^{dxy} is

$$\sigma_{zz}^{dxy}(\theta, \phi = 0°) = \sigma_{zz}^{0} \sum_{\nu=-\infty}^{\infty} \frac{1}{16} \frac{\left(J_{\nu-2}(ak_F \tan\theta) - J_{\nu+2}(ak_F \tan\theta)\right)^2}{1 + (\nu\omega_0\tau \cos\theta)^2}. \tag{4.3.8}$$

Since the term for $\nu = 0$ in the summation vanishes, the ADMRO amplitude is small.

4.3.4 d_{xx}-Type Corrugation

We consider the ADMRO effect of the Fermi surface illustrated in Fig. 4.2.1-(d). It is similar to the s-type corrugation but the corrugation is flat at $k_x = 0$. Fig. 4.3.1-(d) shows the numerically calculated $\rho_{zz}(\theta)$ for different values of ϕ. It is seen that the overall shape of the curves is similar to that for s-type corrugation but the amplitude as well as the peak position of the oscillation depend on ϕ. The peak positions shift to higher angles with increasing ϕ. For $\phi = 0°$, the peak of the oscillation occurs at $\theta \sim 31°$,61°,71°,*etc.* while it occurs at $\theta \sim 53°$, 67°, 73°, *etc.* for $\phi = 90°$. The peaks and valleys at higher angles are inverted between curves at $\phi = 0°$ and 90°. The final expression of σ_{zz}^{dxx} for $\phi = 0°$ is

$$\sigma_{zz}^{dxx}(\theta, \phi = 0°) = \sigma_{zz}^{0} \sum_{\nu=-\infty}^{\infty} \frac{1}{16} \frac{\left(J_{\nu-2}(A) + J_{\nu+2}(A) - 2J_{\nu}(A)\right)^2}{1 + (\nu\omega_0\tau \cos\theta)^2} \tag{4.3.9}$$

where $A = ak_F \tan\theta$. In the high field limit, eq.(4.3.9) becomes

$$\sigma_{zz}^{dxx}(\theta, \phi = 0°) \approx \frac{\sigma_{zz}^{0}}{4} \left(J_2(ak_F \tan\theta) - J_0(ak_F \tan\theta)\right)^2. \tag{4.3.10}$$

The *zeros* of $(J_0(A) - J_2(A))$ occur at approximately the same positions as those of $J_0(A)$ for $A \gg 1$, so that the peak angle of the oscillation is given by eq.(2.5.13).

For $\phi = 90°$, on the other hand, the analytic expression for σ_{zz}^{dxx} is

$$\sigma_{zz}^{dxx}(\theta, \phi = 90°) = \sigma_{zz}^{0} \sum_{\nu=-\infty}^{\infty} \frac{1}{16} \frac{\left(J_{\nu-2}(A) + J_{\nu+2}(A) + 2J_{\nu}(A)\right)^2}{1 + (\nu\omega_0\tau \cos\theta)^2}. \tag{4.3.11}$$

The high field asymptotic form of σ_{zz}^{dxx} is determined by the $\nu = 0$ term in the summation,

$$\sigma_{zz}^{dxx}(\theta, \phi = 90°) \approx \frac{\sigma_{zz}^{0}}{4} (J_2(ak_F \tan\theta) + J_0(ak_F \tan\theta))^2. \tag{4.3.12}$$

The *zeros* are approximately given by the condition,

$$ak_F \tan\theta_n = \pi\left(n + \frac{1}{4}\right) \quad \text{for} \quad n \gg 1, \quad n : \text{integer}. \tag{4.3.13}$$

This condition is the same as eq.(4.3.1), except that the first peak is missing. Inverted peaks occur for large n as compared to the s-type corrugation.

4.3.5 Discussion

We have studied the angular dependence of magnetoresistance for four types of cylindrical Fermi surface with different corrugation symmetries. It has been shown that the ADMRO effect exhibits significant variations depending on the type of the corrugation symmetry. We summarize the characteristics of the ADMRO effect for each Fermi surface in terms of (a) the ϕ-dependence and (b) the behavior of the peak angles θ_n.

(a) For the s-type corrugation, the ADMRO is independent of ϕ. For the p- or d_{xy}-type corrugation the ADMRO effect becomes much weaker for special values of ϕ. The ADMRO for the p-type corrugation has a two-fold symmetry with respect to the azimuthal angle ϕ, and the d_{xy}-type corrugation has a four-fold symmetry. The ADMRO effect for the d_{xx}-type corrugation also exhibits a two-fold symmetry in ϕ.

(b) The peak angles θ_n of the ADMRO for the s-type corrugation is given by eq.(2.5.13). The phase factor in the ($\tan\theta$ vs. n) plot is $(-\pi/4)$. For the p-type corrugation, the ADMRO exhibits an inverted peak structure as compared with the s-type case. The peak positions for large n are given by eq.(4.3.1) and the phase factor is $(-3\pi/4)$. For the d_{xy}-type corrugation a peak occurs at $\theta = 0°$, but the peak angles θ_n for large n are approximately the same as the s-type case so that the phase factor is $(-\pi/4)$. Thus the ($\tan\theta$ vs. n) plot has

a significant deviation from linearity at small n. For the d_{xx}-type corrugation, both the peak position and the phase factor depend on ϕ. The phase factor for $\phi = 0°$ is $(-\pi/4)$ for large n, and that for $\phi = 90°$ is $(\pi/4)$.

Thus we can extract useful information on the corrugation symmetry of a cylindrical Fermi surface from the ϕ-dependence and the phase factor of the ADMRO.

We comment on the possible relevance of the present results to the inverted ADMRO observed in (BEDT-TTF)$_2$TlHg(SCN)$_4$ and (BEDT-TTF)$_2$KHg(SCN)$_4$. Kartsovnik *et al.*[7] have investigated the ADMRO in (BEDT-TTF)$_2$TlHg(SCN)$_4$ by two-axis rotation of magnetic field. The ADMRO in this material shows an inverted peak structure. It is also strongly dependent on ϕ,*i.e.* the ADMRO effect which is the largest at $\phi \approx \phi_{\max}$ disappears at $\phi \approx (\phi_{\max} \pm 90°)$. It was also seen that the peak positions are approximately proportional to $\tan\theta_n$. (*i.e.* $\tan\theta_n \propto n$) They have discussed the inverted ADMRO effect in the light of the angular dependent commensurability effect in open orbit of a quasi-one-dimensional Fermi surface.[12]

We have shown that a p-type symmetry of corrugation of a cylindrical Fermi surface can lead to an inverted peak structure of the ADMRO effect. This may explain the basic features of the "inverted " ADMRO observed in (BEDT-TTF)$_2$TlHg (SCN)$_4$ and (BEDT-TTF)$_2$ KHg(SCN)$_4$. Whether or not the corrugation symmetries considered here are appropriate for these materials has to be judged by further experimental studies and band calculations. The ADMRO in these materials, however, has additional features that are not explained with the present model. First, the periodicity in $\tan\theta$ increases with increasing ϕ, roughly as $\sim 1/\cos\phi$. Secondly, the ADMRO curve is such that it has downward cusps, *i.e.* the change in resistivity is much sharper near the valleys than near the peaks. While the former feature may be explained by considering a cylindrical Fermi surface with an highly-elongated elliptic cross-section, the latter seems more difficult to explain.

To summarize, we have shown that types of corrugation symmetry for a cylindrical Fermi surface can give rise to a variety of the ADMRO effect differing in its phase factor and in its dependence on

the azimuthal angle. In particular, the behavior for the p-type corrugation may have some relevance to the inverted peak structure of the ADMRO experimentally observed in some organic conductors.

References

1) K.Kajita, Y.Nishio, T.Takahashi, W.Sasaki, R.Kato, H.Kobayashi, A.Kobayashi and Y.Iye: Solid State Commun., **70**(1989)1189.
2) M.V.Kartsovnik, P.A.Kononovich, V.N.Laukhin and I.F.Shchegolev: Sov. Phys. JETP Lett., **48**(1988)541.
3) K.Yamaji: J. Phys. Soc. Jpn., **58**(1989)1520.
4) R.Yagi, Y.Iye, T.Osada and S.Kagoshima: J. Phys. Soc. Jpn., **59**(1990)3069.
5) R.Yagi, Y.Iye, Y.Hashimoto, T.Odagiri, H.Noguchi, H.Sakaki and T.Ikoma: J. Phys. Soc. Jpn., **60**(1990)3784.
6) T.Osada, R.Yagi, A.Kawasumi, S.Kagoshima, N.Miura, M.Oshima and G.Saito: Phys. Rev., **B41**(1990)5428.
7) M.V.Kartsovnik, A.E.Kovalev, V.N.Laukhin and S.I.Peotskii: J. Phys. I France, **2**(1992)223.
8) R.W.Winkler, J.P.Kotthaus and K.Ploog: Phys. Rev. Lett., **62**(1989)1177.
9) R.R.Gerhardts, D.Weiss, K.v.Klitzing: Phys. Rev. Lett., **62**(1989)1173.
10) R.Yagi and Y.Iye: submitted to J. Phys. Soc. Jpn.
11) J.M.Ziman: *"Principles of The Theory of Solids"*, (Cambridge University Press, Cambridge,1972) 2nd ed., p.301.
12) T.Osada, A.Kawasumi, S.Kagoshima, N.Miura and G.Saito: Phys. Lev. Lett., **66**(1991)1525.

Chapter 5
Historical Survey

Oscillatory Magnetoresistance in Two-Dimensional Electron Systems Subject to Modulated Structures

5.1 Weiss Oscillation in Two-Dimensional Electron Systems

The energy spectrum of an electron system under the influence of both a periodic potential and a magnetic field has long been a fascinating, but only theoretical subject. Recent development of microfabrication technique and availability of high mobility two-dimensional electron systems in semiconductor heterostructures has brought the subject to the experimental feasibility.

Recently, a novel type of oscillatory magnetoresistance has been demonstrated in the two-dimensional electron system subject to a periodic potential by Winkler *et al.*[1] and Gerhardts *et al.*[2], which is often called Weiss oscillation. The magnetoresistance oscillation occurs as a result of the interference between the cyclotron motion and the spatial period of the electric potential. The potential modulation was realized by different methods by the two groups. Winkler *et al.*[1] formed a one-dimensional periodic potential by a modulated metal gate structure as illustrated in Fig. 5.1.1. Gerhardts *et al.* used a holographic interference pattern of laser and formed the periodic potential modulation exploiting the persistent photoconductivity.

Figure 5.1.2 shows the data of magnetoresistance by Gerhardts *et al.* Two types of oscillation are seen. The rapid oscillations in higher fields are due to the usual SdH effect. The oscillations in the lower fields are the Weiss oscillation. We can summarize the salient features of this oscillation as follows:

1) Oscillation is periodic in $1/B$. But it differs from the SdH effect.
2) It survives much higher temperatures as contrasted to the SdH effect.

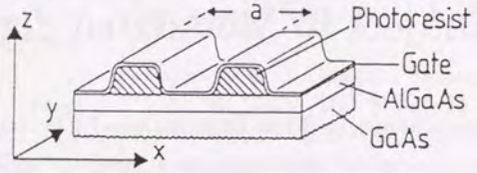

Fig.5.1.1 Sample structure for one dimensional potential modulation. (After Winkler *et al.*[1])

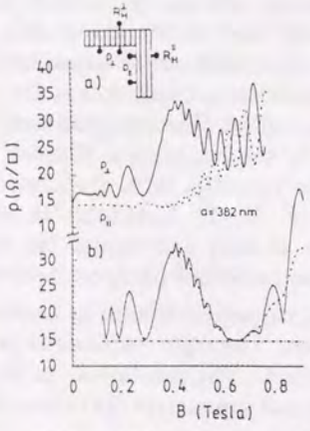

Fig.5.1.2 (a) Magnetoresistance as a function of magnetic field. The rapid oscillations in $\rho_\perp(\rho_{xx})$ in low fields are due to Weiss oscillation. $N_s = 3.16 \times 10^{11}\text{cm}^{-2}$, $\mu = 1.3 \times 10^{-6}\text{cm}^2/\text{Vs}$, $a = 382$ nm and $T = 2.2$K. (b) Calculation for $T = 2.2$K and for 4.2K using V_0=0.3 meV. (After Gerhardts *et al.*[2])

3) The oscillation is dependent on the current direction. The oscillation in ρ_{xx} is larger than that in ρ_{yy}. (The x-axis is the direction of potential modulation.)

5.2 Explanation

The physical origin of the magnetoresistance oscillation is discussed by Winkler *et al.*[1] and Gerhardts *et al.*[2] We consider a periodic electric potential modulation $V(x)$ in x-direction with period d, $\left(V(x) = V\cos(Kx), K = 2\pi/d\right)$, and the magnetic field B in z-direction. The vector potential in the Landau gauge is $\vec{A} = (0, Bx, 0)$. The Schödinger equation is

$$\left\{-\frac{\hbar^2}{2m}\frac{\partial^2}{\partial x^2} + \frac{e^2B^2}{2m}(x - x_0)^2 + V_0\cos(Kx)\right\}\phi(x) = E\phi(x). \quad (5.2.1)$$

Here, $x_0 = -l_B^2 k_y$,$(l_B = \sqrt{\hbar/eB})$. The first order perturbation theory gives the energy spectrum for a weak electric potential modulation as

$$E(N, k_y) = \left(N + \frac{1}{2}\right)\hbar\omega + < N, k_y|V(x)|N, k_y > + \cdots. \quad (5.2.2)$$

The presence of the periodic potential lifts the degeneracy of Landau subband by the matrix element term in eq.(5.2.2).

To evaluate the matrix element, different methods are taken. One is the explicit evaluation, and the other is to approximate the matrix element by a semiclassical expectation value. These methods result in the same though slightly different functional form.

The semiclassical approximation is based on the assumption that the cyclotron motion is only slightly perturbed by the presence of the potential modulation. For this case, the semiclassical trajectory of an electron can be written by $(R_c\cos(\omega t) + x_0, R_c\cos(\omega t) + y_0)$, where (x_0, y_0) is a center coordinate of the cyclotron motion. The expectation value for the spatially varying potential is

$$< V(x) > = \frac{1}{T}\int_0^T V_0\cos(Kx)dt \quad (5.2.3)$$

$$= \int_{x_0 - R_c}^{x_0 + R_c} \frac{V_0\cos(Kx)}{\pi\sqrt{R_c^2 - (x - x_0)^2}}dx. \quad (5.2.4)$$

Here, $R_c = \hbar k_F/eB$ is the cyclotron radius. We obtain the results of eq.(5.2.2) as follows:

$$E(N, k_y) = \left(N + \frac{1}{2}\right) + V_0 J_0(KR_c)\cos(Kx_0). \tag{5.2.5}$$

Since $J_0(z)$ is approximated by eq.(2.5.12), the Landau subband becomes dispersionless when the cyclotron radius satisfies the condition,

$$2R_c = d\left(n - \frac{1}{4}\right). \tag{5.2.6}$$

The matrix element in eq.(5.2.2) can be also calculated by integration with eigen function. The result is

$$E(N, x_0) = \left(N + \frac{1}{2}\right)\hbar\omega + V_0\cos(Kx_0)\mathrm{e}^{-X/2}L_N(X). \tag{5.2.7}$$

Here,$X = \frac{1}{2}K^2l_B^2$, and L_N are the N-th order Laguerre polynomials. The *zeros* ($L_N(X) = 0$) of the Laguerre polynomials are given by

$$X \approx \frac{\left[\frac{1}{2}\pi(\lambda - 1/4)\right]^2}{N + (1/2)} \qquad \lambda\text{:integer.} \tag{5.2.8}$$

The flat subband condition occurs when eq.(5.2.6) is satisfied. Since the correction to the Drude conductivity form these magnetic band conduction is written as

$$\begin{aligned}\delta\sigma_{yy} &= \frac{e^2\tau}{\hbar\omega}\int\frac{dk_y}{\pi}v_y^2 \\ &\approx \frac{2m^*e\tau}{\pi\hbar^3}\frac{V_0^2}{Ba}\frac{\cos^2[(2\pi R_c/a) - \pi/4]}{(2\pi n_e)^{1/2}},\end{aligned} \tag{5.2.9}$$

in high temperature approximation, the oscillations appear in ρ_{xx} since $\rho_{xx} = \sigma_{yy}/(\sigma_{xy}^2 + \sigma_{yy}\sigma_{xx}) \approx \sigma_{yy}/\sigma_{xy}^2$ for $\omega\tau \gg 1$. Here, v_y is $(1/\hbar)(\partial E/\partial k_y)$. Thus oscillatory magnetoresistance arises from the periodic occurrence of flat Landau subbands.

Another explanation of the oscillation in a semiclassical picture is given by Beenakker[3]. He has shown that the oscillation arise from the periodic quenching of the electron drift.

An electron executes a so-called $\vec{E}\times\vec{B}$ drift in magnetic field under the influence of the electric field, with the drift velocity $\vec{v}_{\mathrm{drift}} = \vec{E}\times\vec{B}/|\vec{B}|^2$. When the amplitude of the spatially varying potential is weak and the cyclotron radius is sufficiently large (*i.e.* $R_c \gg d$, and $E_F \gg V_0$), we can treat the cyclotron motion and the $\vec{E}\times\vec{B}$drift separately. Since $\vec{E}$ is given by $(1/e)\nabla V(x)$, the spatially varying electric field is formulated as $\vec{E} = (-\frac{V_0K}{e}\sin(Kx), 0, 0)$. The corresponding drift velocity is

$$v_{\mathrm{drift}} = \frac{V_0K}{eB}\sin(Kx) \tag{5.2.10}$$

in the y-direction. The resulting drift velocity under a modulated electric potential is obtained by averaging over a trajectory of a cyclotron motion.

$$\begin{aligned}\bar{v}_{\mathrm{drift}} &= \frac{1}{2\pi}\int_0^{2\pi}\frac{-E_x(x_0 + R_c\cos\phi)}{B}d\phi \\ &= \frac{1}{2\pi}\int_0^{2\pi}\frac{V_0K}{eB}\sin(KR_c\cos\phi + Kx_0)d\phi \\ &= \frac{V_0K}{eB}\sin(Kx_0)J_0(R_cK).\end{aligned} \tag{5.2.11}$$

The averaged drift velocity vanishes for $J_0(R_cK) = 0$, regardless of the guiding center co-ordinate x_0. This leads to the oscillatory magnetoresistance.

5.3 The Weiss Oscillation and the ADMRO Effect

Here we comment on the relation between the Weiss oscillation in a two-dimensional system and the ADMRO effect in a quasi-two-dimensional system.

In the case of the Weiss oscillation, the periodic electric potential modulation causes a $E \times B$ drift. The $E \times B$ drift averaged over a trajectory (eq.(5.2.11)) vanishes when eq.(5.2.6) is satisfied. The number of the potential peaks electrons feel in a cyclotron motion varies with the cyclotron radius and hence with field intensity.

For the case of ADMRO effect, the Fermi surface corrugation is related with the group velocity by $v_z = (1/\hbar)(\partial E/\partial k_z)$. As seen in eq.(2.5.11), the group velocity averaged over a trajectory vanishes when eq.(2.5.13) is satisfied. The number of corrugation of the Fermi surface which electron experiences during a cyclotron motion is determined by the angle of the magnetic field.

References

1) R. W. Winkler, J. P. Kotthaus and K. Ploog: Phys. Rev. Lett., **62**(1989)1177.
2) R. R. Gerhardts, D. Weiss, K.v.Klitzing: Phys. Rev. Lett., **62**(1989)1173.
3) C. W. J. Beenakker: Phys. Rev. Lett., **62**(1989)2020.
4) K. Yamaji: J. Phys. Soc. Jpn., **58**(1989)1520.
5) R. Yagi, Y. Iye, T. Osada and S. Kagoshima: J. Phys. Soc. Jpn., **59**(1990)3069.
6) T. Osada, R. Yagi, A. Kawasumi, S. Kagoshima, N. Miura, M. Oshima and G. Saito: Phys. Rev., **B41**(1990)5428.

Chapter 6

Oscillatory Magnetoresistance in a Two-Dimensional Electron Systems in a Periodically Modulated Magnetic Field

We have studied energy spectra of a two-dimensional electron system in the presence of a weak magnetic field modulation. It is found that the magnetoresistance shows an oscillatory behavior similar to the so-called Weiss oscillation for the case of an electric potential modulation. The main difference between the two cases is that the phase of the magnetoresistance oscillation is shifted by $\pi/2$. This results in an inverted peak and valley structure for the magnetic field modulation as compared to the Weiss oscillation.

6.1 Introduction

In this Chapter, we investigate the effect of magnetic modulation to the two-dimensional electron gas. Experimentally as well as theoretically, the two-dimensional electron system in a magnetic field modulation is less explored in comparison to the electric potential modulation. Yoshioka and Iye[9] studied the case of two-dimensionally modulated magnetic field. We investigate the energy spectrum of a two-dimensional electron system in the presence of a one-dimensionally modulated magnetic field and we discuss in the light of the Weiss oscillation.

This Chapter is organized as follows. In the next section, we define the model and the Schrödinger equation to be solved. The results of calculations, both numerical and analytic, are presented and discussed in Sec.6.3. In Sec.6.4, we describe our experimental efforts to observe the predicted effect. Section 6.5 is devoted to summary and concluding remarks.

6.2 Model

We consider a two-dimensional electron gas subject to a perpendicular magnetic field whose strength is one-dimensionally modulated with a period d. We take the two-dimensional plane as the xy-plane, with the x-axis along the direction of modulation. The magnetic field is expressed as $\vec{B} = \big(0, 0, B_0 + B_1 \cos(Kx)\big)$, where $K = 2\pi/d$, B_0 is the uniform field and B_1 denotes the field modulation amplitude. The corresponding vector potential is, in the Landau gauge, $\vec{A} = \big(0, B_0 x + (B_1/K)\sin(Kx), 0\big)$. The Schrödinger equation for the two-dimensional electrons is

$$\Big\{-\frac{\hbar^2}{2m}\frac{\partial^2}{\partial x^2} + \frac{1}{2m}\Big(-\mathrm{i}\hbar\frac{\partial}{\partial y} - eB_0 x - \frac{eB_1}{K}\sin(Kx)\Big)^2$$

$$-g\mu_B S\big(B_0 + B_1\cos(Kx)\big)\Big\}\psi(x,y) = E\psi(x,y). \qquad (6.2.1)$$

Here, g is the g-factor, μ_B is the Bohr magneton and $S(=\pm\frac{1}{2})$ is the spin quantum number. Using $\psi(x,y) = \exp(-\mathrm{i}k_y y)\phi(x)$, eq.(6.2.1) is reduced to a one-dimensional form,

$$\Big\{-\frac{\hbar^2}{2m}\frac{\partial^2}{\partial x^2} + \frac{1}{2m}\big(\hbar k_y + eB_0 x + \frac{eB_1}{K}\sin(Kx)\big)^2$$

$$-g\mu_B S\big(B_0 + B_1\cos(Kx)\big)\Big\}\phi(x) = E\phi(x). \qquad (6.2.2)$$

In order to make the discussion transparent, we shall treat the orbital effect and the Zeeman effect of the modulated magnetic field, separately.

6.3 Results and Discussion

6.3.1 Numerical Solution - Orbital Effect

We first consider the case of pure orbital effect. We drop off the Zeeman term from eq.(6.2.2), and solve it numerically to obtain the energy eigenvalues as a function of the guiding center coordinate $x_0 = -k_y l_B^2$, ($l_B \equiv (\hbar/eB_0)^{\frac{1}{2}}$ is the magnetic length). The presence

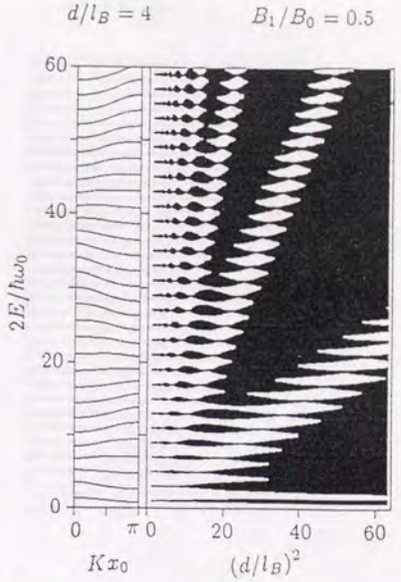

Fig.6.3.1 Left Panel: Numerical solution of the energy eigenvalues for the orbital effect of magnetic field modulation. The parameter values for the figure are $(d/l_B) = 4$ and $(B_1/B_0) = 0.5$. Landau levels lose the dispersion for $2E/\hbar\omega_0 = 7$, 20,40. Right Panel: Evolution of the energy eigenvalues as a function of $(d/l_B)^2$, for the same magnetic field modulation amplitude. The flat band condition is $2R_c = d(n-3/4)$.

of magnetic field modulation lifts the degeneracy of Landau levels to yield an energy dispersion as a function of the guiding center coordinate x_0.

The left panel of Fig.6.3.1 shows the dispersion of the Landau subbands for $d/l_B = 4$, $B_1/B_0 = 0.5$. It is seen that the subband width varies with $2E/\hbar\omega_0$, ($\omega_0 = eB_0/m$). For this figure, the flat band condition occurs at $2E/\hbar\omega_0 \approx 7$, 20 and 40.

The right panel shows the evolution of the energy spectrum with

Fig.6.3.2 Numerical solution of the energy eigenvalues for the orbital effect, for a smaller modulation amplitude, $B_1/B_0 = 0.1$. The flat band position is the same as Fig.1.

$(d/l_B)^2$. The ratio $B_1/B_0 = 0.5$ is fixed for this calculation. The subband width oscillates as a function of $(d/l_B)^2$. Flat subbands occur periodically at the condition given by

$$\left(\frac{2E}{\hbar\omega_0}\right) = \frac{1}{4}\left(n - \frac{3}{4}\right)^2 \left(\frac{d}{l_B}\right)^2, \quad n : \text{integer}. \tag{6.3.1}$$

An equivalent formula is

$$2R_c = d(n + \delta), \quad \delta = -\frac{3}{4}, \quad n : \text{integer}. \tag{6.3.2}$$

By the same argument as the case of the Weiss oscillation, the periodical occurrence of flat band condition leads to an oscillatory magnetoresistance. The hallmark of the present effect as contrasted to the

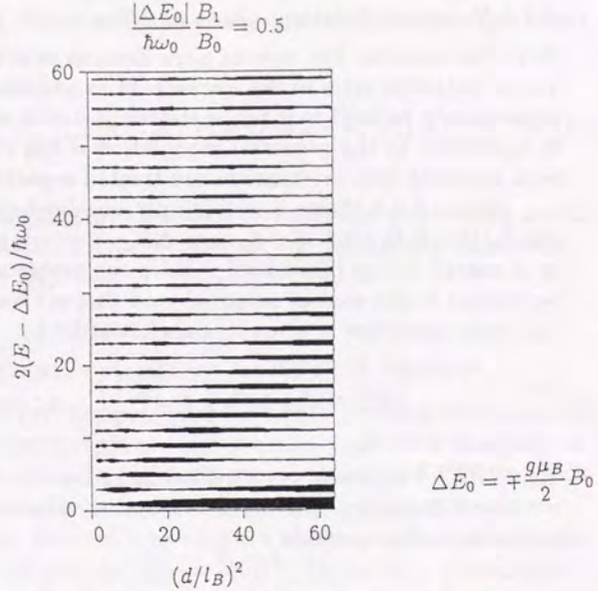

Fig 6.3.3 Numerical solution of the energy eigenvalues for the Zeeman effect. The parameter values are indicated in the figure. The flat band condition is $2R_c = d(n - 1/4)$ which is the same as that for the Weiss oscillation.

Weiss oscillation is the change in the phase of the oscillation by $\pi/2$, namely the positions of peaks and valleys are interchanged.

Figure 6.3.2 shows a similar result for a weaker magnetic field modulation, $B_1/B_0 = 0.1$. The Landau subband dispersion becomes smaller because of the smaller amplitude of modulation. The condition for the occurrence of flat band, however, remains the same as Fig.6.3.1. Equation (6.3.2) for the flat band condition is independent of the modulation amplitude as long as the modulation is not too strong. Discussion on the case of strong modulation is deferred to the end of this section.

6.3.2 Numerical Solution - Zeeman Effect

Next, we consider the case of pure Zeeman effect by neglecting the vector potential term in the momentum expression in eq.(6.2.2). It is immediately noticed that the spatial modulation of the Zeeman term is equivalent to the potential modulation if two electron subsystems with opposite spin orientations are treated separately.

Figure 6.3.3 shows a numerically obtained energy spectrum for $(|\Delta E_0|/\hbar\omega_0)(B_1/B_0) = 0.5$, here $\Delta E_0 = -(+)g\mu_B B_0/2$ is the Zeeman energy for up (down) spin. Since the problem is mathematically equivalent to the case of potential modulation (Weiss oscillation), the flat band condition is given straightforwardly by

$$2R_c^{\pm} = d(n+\delta), \quad \delta = -\frac{1}{4}, \quad n : \text{integer}. \tag{6.3.3}$$

Here, $R_c^{+(-)}$ represents the cyclotron radius for the up(down) spin electron subsystem. This leads to magnetoresistance oscillations with two independent periods.

6.3.3 Analytical Results

In this section, we solve eq.(6.2.2) analytically with a simplifying assumption. When the magnetic field modulation is weak, the energy eigenvalues are given by a perturbation as

$$E(N,x_0) = \left(N+\frac{1}{2}\right)\hbar\omega_0 + < N,x_0|V|N,x_0 > + \cdots. \tag{6.3.4}$$

We approximate the second term by the semiclassical expectation value of V. For the case of the orbital effect, retaining only the term first order in (B_1/B_0K), eq.(6.3.4) becomes

$$E(N,x_0) \approx \left(N+\frac{1}{2}\right)\hbar\omega_0 + \frac{e^2}{m}\frac{B_0B_1R_c}{K}\cos(Kx_0)J_1(KR_c). \tag{6.3.5}$$

The flat band condition is given by *zeros* of the first order Bessel function, $J_1(KR_c) = 0$. For sufficiently large KR_c, the *zeros* occur at

$2R_c = d(n-3/4)$. For the Zeeman energy modulation, the eigenvalues are

$$E(N,x_0) \approx \left(N+\frac{1}{2}\right)\hbar\omega_0 \mp \frac{g\mu_B}{2}\left[B_0 + B_1\cos(Kx_0)J_0(KR_c^{\pm})\right]. \tag{6.3.6}$$

The flat band condition in this case is given by the *zeros* of the zeroth order Bessel function $J_0(KR_c^{\pm})$. Again for sufficiently large $KR_c^{\pm}$, this translates to $2R_c^{\pm} = d(n-1/4)$.

6.3.4 Simple Physical Interpretation for the Peak Inversion

As mentioned earlier, the principal difference between the magnetic field modulation (orbital effect) and the scalar potential modulation(Weiss oscillation) lies in the positions of peaks and valleys. This difference can be easily understood by the following argument.

The magnetic field modulation gives rise to an effective potential $(e^2/2m)(B_0x + (B_1/K)\sin(K(x+x_0)))^2$. For a weak modulation ($|B_1/B_0| \ll 1$), the dominant contribution comes from the first order term, $(e^2/m)(B_0B_1/K)x\sin(K(x+x_0))$. This means that the effective potential modulation term changes its phase by π at $x = 0$. The phase jump occurs because the Lorentz force changes its sign depending on the sign of the electron velocity. The effect of inverted phase between $+x$ and $-x$ on the eigen function results in the phase shift by $\pi/2$ from the case of ordinary potential modulation.

In the present case, we can also explain the effect by the guiding center drift motion picture as discussed by Beenakker[3] for the case of scalar potential modulation. We describe the electron motion for a uniform magnetic field as $(x,y) = (R_c\cos(\omega_0 t)+x_0, R_c\sin(\omega_0 t)+y_0)$, where (x_0,y_0) denotes a center of a cyclotron motion. If we assume a sufficiently weak magnetic field modulation ($B_1 \ll B_0$), then we can treat cyclotron motion and the orbital center drift motion separately. We define a equivalent electric field for a magnetic field modulation as $(\vec{v}\times\vec{B}_{\rm mod})$, and apply the $\vec{E}\times\vec{B}$ drift motion in a uniform magnetic field. Here $\vec{B}_{\rm mod} = (0,0,B_1\cos(Kx))$ is the spatially varying component of the magnetic field and $\vec{v}$ is the electron velocity. The

time averaged drift velocity, $\vec{v}_{\rm drift} = (\bar{v}_x, \bar{v}_y)$ is expressed as

$$\begin{aligned}\bar{v}_y &= -\frac{1}{T'}\frac{B_1 R_c \omega_0}{B_0}\int_0^{T'} \cos(Kx)\cos(\omega_0 t)\mathrm{d}t \\ &= \frac{e}{m} B_1 R_c J_1(KR_c)\sin(Kx_0),\end{aligned} \tag{6.3.7}$$

$$\begin{aligned}\bar{v}_x &= \frac{1}{T'}\frac{B_1 R_c \omega_0}{B_0}\int_0^{T'} \cos(Kx)\sin(\omega_0 t)\mathrm{d}t \\ &= 0.\end{aligned} \tag{6.3.8}$$

Here, $T'(=2\pi/\omega_0)$ is the period of the cyclotron motion. Non-vanishing cyclotron-motion-center drift occurs only in the y-direction. For $J_1(KR_c) = 0$ in eq.(6.3.7) the drift velocity vanishes regardless of x_0. When R_c satisfies the condition, the guiding center drift is quenched and hence σ_{yy} takes a minimum. The Landau subband dispersion for eq.(6.3.5) arises from this guiding center drift motion. Equation (6.3.7) can be also derived from $v_y = (1/\hbar)(\partial E/\partial k_y)$ with E given by eq.(6.3.5).

6.3.5 Strong Modulation

In the above, we treated the case of weak magnetic field modulation. Here we discuss the case of strong modulation, such that $B_1/B_0 \approx 1$. We only consider the orbital effect, since the Zeeman effect does not give anything particularly new.

Figure 6.3.4 shows a numerically obtained subband structures for four different values of B_1/B_0. It is seen that the flat bands become less distinct with increasing modulation amplitude. It is also recognized that a new branch becomes increasingly well defined for $B_1/B_0 > 1$. For $B_1/B_0 = 2$ (the right most panel), the branch becomes almost continuous. This new branch is attributed to the bound state formed within the local minima of the strongly modulated potential. As seen in the figure, this state has a large dispersion and therefore can give a large contribution to the electrical transport in high fields. In such a case, the band conductivity correction to σ_{yy} is dominated by this state, so that the oscillatory magnetoresistance is masked. Since the Lorentz force depends on the velocity as well as

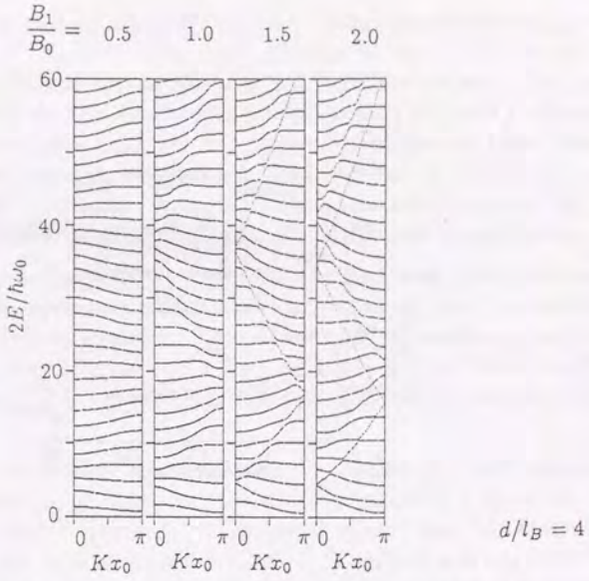

Fig.6.3.4 Numerical solution of the energy eigenvalues for the orbital effect for four different values of field modulation amplitude. With increasing modulation, the flat band becomes less discernible and new branches emerge.

on the field intensity, the case of the sufficiently large Fermi energy (Fermi velocity) may result in a similar effect.

6.4 Experimental Attempt

We describe our current experimental attempt to observe the oscillatory magnetoresistance due to magnetic field modulation by using a two-dimensional electron gas (2DEG) in a GaAs/AlGaAs heterostructure. The device structure (Device M) is depicted in the inset of Fig.6.4.1. The structure is basically the same as the standard high electron mobility transistor (HEMT), except that the gate electrode is lithographically patterned. Since we do not want a scalar poten-

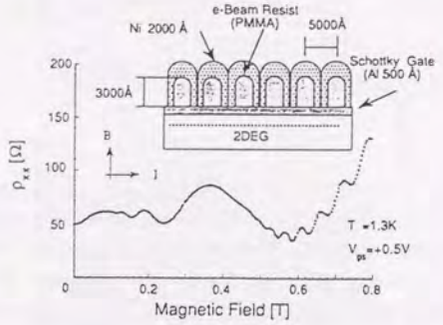

Fig.6.4.1 Magnetoresistance measurement of a two dimensional electron gas in GaAs/AlGaAs heterostructure with a stripline-magnetic metal gate (Device M). The sample structure is illustrated in the inset. The oscillations in the low field regime arise from the metal gate structure, while those at higher fields are the Shubnikov-de Haas effect. Details are discussed in the text.

tial modulation, a uniform layer (500Å thick Al) of a non-magnetic metal is first deposited on the surface of a GaAs/AlGaAs single heterostructure to form a Schottky gate. The surface is covered by an electron beam resist and a stripline array (periodicity 5000Å, line width 2500Å) is defined by electron beam lithography. A layer (2000Å thick) of ferromagnetic metal (Ni) is then deposited. The distance between the 2DEG and the bottom of the magnetic layer is $\sim$ 1000Å. With this structure, an externally applied uniform magnetic field is spatially modulated at the plane of 2DEG.

The main part of Fig.6.4.1 shows a magnetoresistivity ρ_{xx} of Device M at T = 1.3K. The areal density of the 2DEG is n_e = $3.9 \times 10^{11}\mathrm{cm}^{-2}$, and the mobility is $3.2 \times 10^5\mathrm{cm}^2/\mathrm{Vsec}$. The current is passed along the direction of modulation. The rapid resistance oscillation above B = 0.5T are due to the Shubnikov-de Haas effect. The oscillatory features in the lower field regime (B <0.6T) are attributed to the modulated structure. The same result is obtained in the devices with ferromagnetic stripline gate formed by permalloy.

Further investigation, however, has clarified that the major part of the low-field oscillatory magnetoresistance has its origin other than the magnetic field modulation. The positions of the peaks and valleys are found to obey the condition $2R_c = d(n - \frac{1}{4})$ for Weiss oscillation rather than that expected for the orbital effect of magnetic field modulation.

We have examined the oscillation by preparing three different devices. Device A as depicted in the right panel of Fig. 6.4.2-(a) has the same device structure as Device M except that the magnetic metal is replaced by a nonmagnetic metal (Al). Device B has only the patterned electron beam resist as depicted in Fig. 6.4.2-(b). Device C has no modulated structure on the metal gate as depicted in Fig 6.4.2-(c). The patterned resist of Device C was removed after electron beam deposition.

The left panel of Fig. 6.4.2-(a) shows magnetoresistance of Device A. In the absence of the magnetic stripline metal structure, we can see essentially the same oscillatory magnetoresistance as Fig. 6.4.1 with a comparable amplitude. The left panel of Fig. 6.4.2-(b) shows magnetoresistance of a Device B. The low field oscillation is still visible with only the patterned electron beam resist. The left panel of Fig. 6.4.2-(c) shows magnetoresistance of Device C. For this Device, the low field magnetoresistance oscillation is no longer visible.

The oscillation in Fig. 6.4.1 does not arise from magnetic field modulation because we could see the same oscillation in Device A and B. One of the possible origin for the electric potential modulation is the formation of defects by electron beam deposition. This however is excluded by the fact that Device C exhibits no Weiss oscillation-like effect. Considering that the electric field potential is

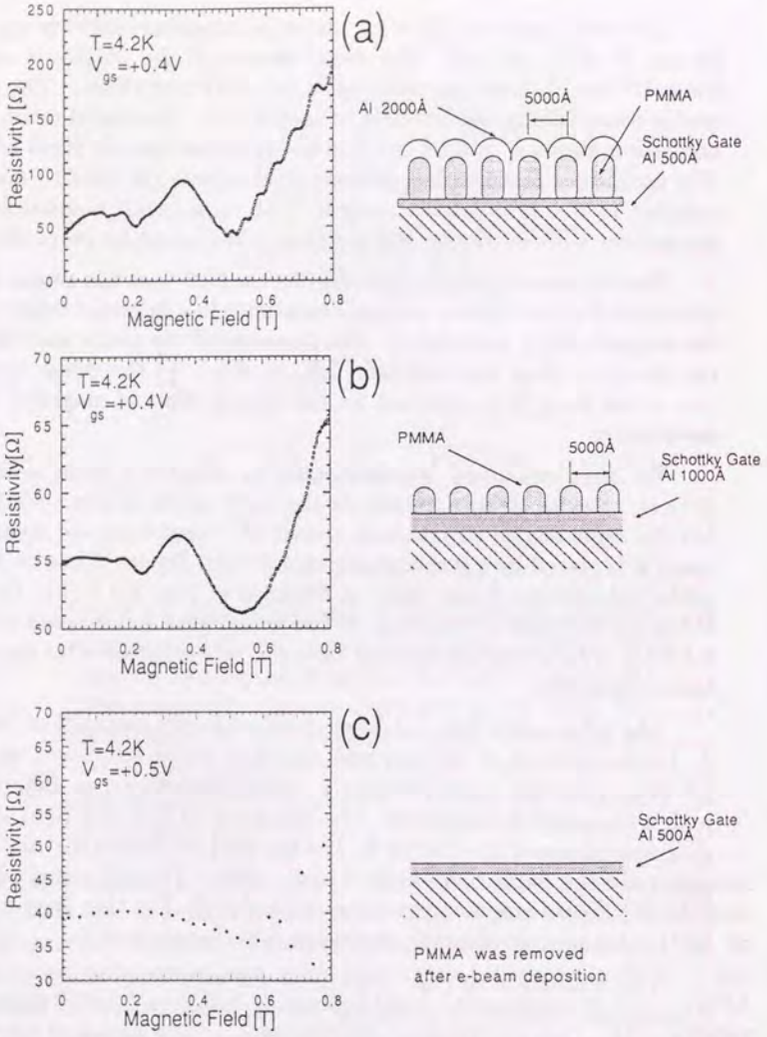

Fig. 6.4.2 Device structure and magnetoresistance of Devices A,B,C. Details are discribed in the text.

made constant at the surface of the GaAs/AlGaAs heterostructure by the presence of a uniform metal gate, the Weiss oscillation-like effect presumably arises from the effective potential formed by spatially modulated strain caused by the presence of the patterned resist and the stripline metal layer.

We estimate the effective electric potential modulation amplitude determined by Fig. 6.4.1 with eq.(5.2.9) is ~ 1 meV. The corresponding value in eq.(6.3.5) for magnetic field modulation $((e^2/m)(B_0 B_1 R_c/K))$ is $\sim 1[\mathrm{meV/T}]\times B_1[\mathrm{T}]$. We estimate that the magnetic field modulation B_1/B_0 in Device M is less than 10 % by a local magnetic field calculation. Thus the magnetic field modulation in Device M is much smaller effect than the observed Weiss oscillation-like effect.

Thus far, our attempt to observe the oscillatory magnetoresistance due to magnetic field modulation is hindered by the dominance of the Weiss oscillation-like effect which possibly arises from the sensitiveness of the 2DEG in our heterostructure to unintentionally introduced strain effect.

6.5 Summary and Concluding Remarks

We have examined the energy spectrum of a two-dimensional electron system subject to a spatially modulated magnetic field, both numerically and analytically. Similar to the case of periodic scalar potential, the modulation gives rise to finite dispersions of the Landau subbands, but the dispersion vanishes whenever the condition given by eq.(6.3.2) is met. This flat band condition occurs periodically as a function of $1/B$ and manifest itself as an oscillatory magnetoresistance phenomenon. The Zeeman effect of a modulated magnetic field is the same as a potential modulation if two subsystems with opposite spin orientations are treated separately. The orbital effect of a modulated magnetic field yields a similar oscillatory magnetoresistance except that the positions of peaks and valleys are interchanged.

We have made an attempt for experimental observation of the predicted phenomenon. So far, the experimental observation is hindered by the dominant Weiss oscillation phenomenon arising possibly from the sensitiveness of the two-dimensional electron system to an inadvertent strain effect.

References

1) R. R. Gerhardts, D. Weiss, K.v.Klitzing: Phys. Rev. Lett., **62**(1989)1173.
2) R. W. Winkler, J. P. Kotthaus and K. Ploog: Phys. Rev. Lett., **62**(1989)1177.
3) C. W. J. Beenakker: Phys. Rev. Lett., **62**(1989)2020.
4) K. Kajita, Y. Nishio, T. Takahashi, W. Sasaki, R. Kato, H. Kobayashi, A. Kobayashi and Y. Iye: Solid State Commun., **70**(1989)1189.
5) M. V. Kartsovnik, P. A. Kononovich, V. N. Laukhin and I. F. Schegole Sov. Phys. JETP Lett., **48**(1988)541.
6) K. Yamaji: J. Phys. Soc. Jpn., **58**(1989)1520.
7) R. Yagi, Y. Iye, T. Osada and S. Kagoshima: J. Phys. Soc. Jpn., **59**(1990)3069.
8) R. Yagi, Y. Iye, Y. Hashimoto, T. Odagiri, H. Noguchi, H. Sakaki and T. Ikoma: J. Phys. Soc. Jpn., **60**(1991)3784.
9) D.Yoshioka and Y.Iye: J. Phys. Soc. Jpn., **56**(1987)448.
10) T. Osada, R. Yagi, A. Kawasumi, S. Kagoshima, N. Miura, M. Oshima and G. Saito: Phys. Rev., **B41**(1990)5428.
11) T. Osada, A. Kawasumi, R. Yagi, S. Kagoshima, N. Miura, M. Oshima, H. Mori, T. Nakamura and G. Saito: Solid State Commun., **75**(1990)901.
12) T. Sasaki, H. Sato and N. Toyota: Syn. Met., **42**(1991)2211.

Chapter 7

Conclusion

7.1 Achievement of this Thesis

In the former part of this thesis we have discussed the angular dependent magnetoresistance oscillation in quasi-two-dimensional electron system.

• In Chapter 2, we have described a semiclassical interpretation of the angular dependent magnetoresistance oscillation (ADMRO) effect recently found in organic conductors. We have calculated magnetoconductivity tensor components of a corrugated cylindrical Fermi surface within the framework of Boltzmann transport theory. The following facts are found and clarified:

i. Overall shape of the angular dependence of magnetoresistance curves could be explained by the Boltzmann transport theory with a corrugated cylindrical Fermi surface.
ii. The ADMRO effect emerges around $\omega\tau \sim 1$.
iii. The ADMRO effect occurs as a result of the angular periodic occurrence of the difference of the high field asymptotic behavior (B-dependence)of magnetoresistance. This occurs from the angular oscillatory change of the conductivity component due to the electron drift in high fields.
iv. The magnitude of the ADMRO depends on the current direction. The ADMRO effect is largest in the resistivity component in the direction perpendicular to the two-dimensional plane.

The last point iv in our results exhibit difference from the experimental results. We have discussed them in the light of the actual experimental situation.

• In Chapter 3, we have demonstrated that the ADMRO effect indeed occurs in quasi-two-dimensional systems. We have tailored corrugated cylindrical Fermi surfaces using GaAs/AlGaAs superlattices. We have prepared two types of devices for the measurement of ρ_{zz} (vertical

transport) and ρ_{xx} (lateral transport) and compared the magneto-transport property. In the superlattice device for vertical transport, we have succeeded to observe the ADMRO effect by conducting the measurement in higher temperatures ($T \sim 30$K). We have also observed that the peak angles of the ADMRO shift lower angles for increased carrier density. On the other hand, the angular dependence of the magnetoresistance of device for lateral transport measurement was featureless except for the SdH effect and the cusp-like structure around $\theta = 90°$ arising from a localization effect. These results are consistent with our expectation described in Chapter 2.

• In Chapter 4, we have discussed a possible origin of an inverted ADMRO effect observed in organic conductors. We have calculated the angular dependence of magnetoresistance of four model cylindrical Fermi surfaces with different corrugation symmetries. The ADMRO effect is strongly dependent on corrugation patterns. The p-type corrugation Fermi surface in our calculation explains some features of the inverted ADMRO effect in organic conductors, such as (1) the occurrence of an inverted peak structure, (2) the absence of the ADMRO effect at $\phi \approx (\phi_{\max} + 90°)$ where $\phi_{\max}$ is the angle where largest ADMRO effect is seen. However the shape of the ADMRO is different in that sharp dips are impressive in the organic conductors while our calculations exhibit sharp peaks. The validity of our calculation in this Chapter will be clarified by further experiments and band calculations.

In the latter part of this thesis we have concerned ourselves with the oscillatory magnetoresistance of a two-dimensional electron system subject to modulated structures. Especially, we have discussed the Weiss oscillation and the related phenomenon in the case of magnetic field modulation.

• In Chapter 6, we have discussed the energy spectra of a two-dimensional electron system in one-dimensionally modulated magnetic field. We have found that the energy spectra exhibit flat Landau subbands similar to the Weiss oscillation. We inferred the magnetoresistance oscillation due to flat Landau subband similar to the Weiss oscillation. The remarkable difference between the Weiss oscillation and the present oscillation is the phase factor of the flat band condition by π. Reflecting this fact, peak structure of the magnetoresistance oscillation in magnetic field modulation is inverted as compared with the Weiss oscillation. The physical picture by a guiding center drift motion was also discussed.

We have also tried to observe the magnetoresistance oscillation using two-dimensional electrons of the GaAs/AlGaAs heterostructure. We have only observed Weiss-like oscillation arising from unintentionally formed electric potential modulation. We have not succeeded in the experimental observation at the present stage.

Appendix A

Appendix A.1 Derivation of σ_{zz} (σ^s_{zz})

In this section derivation of eq.(2.5.14) is given. We assume a weak corrugation limit ($t \ll E_F$). Then we can approximate the phase variable φ by ξ (Appendix A.3) where ξ is defined by $k_x = k\cos\xi$, $k_y = k\sin\xi$, $k = \sqrt{k_x^2 + k_y^2}$. The cyclotron mass m^* and cyclotron frequency ω has a weak dependence on k_0. We further approximate $m^* \approx m/\cos\theta$ and $\omega \approx \omega_0 \cos\theta$.

The z-component of the group velocity for a magnetic field angle θ can be given by

$$\begin{aligned} v_z &= \frac{2ta}{\hbar}\sin(ak_z) \\ &= \frac{2ta}{\hbar}\sin(a(k_0 - k_x\tan\theta)) \\ &\approx \frac{2ta}{\hbar}\sin(a(k_0 - k_F\tan\theta\cos\varphi)). \end{aligned} \tag{A.1.1}$$

in second order in t/E_F.

The velocity in the integrand of the Shockley tube integral is

$$\begin{aligned} &v_z(\varphi)v_z(\varphi-\varphi') \\ &= \frac{4t^2a^2}{\hbar^2}\sin(a(k_0 - k_F\tan\theta\cos\varphi))\sin(a(k_0 - k_F\tan\theta\cos(\varphi-\varphi')) \\ &= \frac{4t^2a^2}{\hbar^2}\{\sin(ak_0)\cos(ak_F\tan\theta\cos\varphi) \\ &\qquad - \cos(ak_0)\sin(ak_F\tan\theta\cos\varphi)\} \\ &\quad \times\{\sin(ak_0)\cos(ak_F\tan\theta\cos(\varphi-\varphi') \\ &\qquad - \cos(ak_0)\sin(ak_F\tan\theta\cos(\varphi-\varphi'))\}. \end{aligned} \tag{A.1.2}$$

First, we integrate the Shockley tube integral with respect to k_0 using the above formulae. Then the tube integral is reduced to the

following form.

$$\sigma_{zz} = \frac{e^2}{4\pi^3\hbar^2}\frac{\cos\theta}{1-\exp(-2\pi/\omega\tau)}\frac{m^*}{\omega}\frac{\pi}{a}\int_0^{2\pi}d\varphi\int_0^{2\pi}d\varphi'\exp(-\varphi'/\omega\tau)$$
$$\times\frac{4t^2a^2}{\hbar^2}\Big\{\sin(ak_F\tan\theta\cos\varphi))\sin(ak_F\tan\theta\cos(\varphi-\varphi'))$$
$$+\cos(ak_F\tan\theta\cos\varphi)\cos(ak_F\tan\theta\cos(\varphi-\varphi'))\Big\}. \qquad (A.1.3)$$

Using Bessel functions (Appendix A.2), eq.(A.1.3) is expanded as follows:

$$\frac{e^2}{4\pi^3\hbar^2}\frac{\cos\theta}{1-\exp(-2\pi/\omega\tau)}\frac{m^*}{\omega}\frac{\pi}{a}\frac{4t^2a^2}{\hbar^2}$$
$$\times\sum_{\nu=-\infty}^{\infty}\sum_{\nu'=-\infty}^{\infty}J_\nu(ak_F\tan\theta)J_{\nu'}(ak_F\tan\theta)\times\int_0^{2\pi}d\varphi\int_0^{2\pi}d\varphi'\mathrm{e}^{-\varphi'/\omega\tau}$$
$$\times\Big\{\cos((\varphi+\frac{1}{2}\pi)\nu)\cos((\varphi-\varphi'+\frac{1}{2}\pi)\nu')$$
$$+\sin((\varphi+\frac{1}{2}\pi)\nu)\sin((\varphi-\varphi'+\frac{1}{2}\pi)\nu')\Big\}. \qquad (A.1.4)$$

Using relation among trigonometrical functions, the integration in eq.(A.1.4) can be done.

$$\int_0^{2\pi}d\varphi\int_0^{2\pi}d\varphi'\exp(-\varphi/\omega\tau)\cos((\nu-\nu')\varphi+\nu'\varphi'+\frac{1}{2}\pi(\nu-\nu'))$$
$$=2\pi\delta_{\nu,\nu'}\int_0^{2\pi}d\varphi'\mathrm{e}^{-\varphi/\omega\tau}\cos(\nu'\varphi')$$
$$=2\pi\delta_{\nu,\nu'}\frac{1/\omega\tau}{\nu'^2+(1/\omega\tau)^2}(1-\mathrm{e}^{-2\pi/\omega\tau}) \quad . \qquad (A.1.5)$$

Here $\delta_{\nu,\nu'}$ is defined by

$$\delta_{\nu,\nu'} = \begin{cases} 1 & \text{for} \quad \nu=\nu' \\ 0 & \text{for} \quad \nu\neq\nu'. \end{cases} \qquad (A.1.6)$$

Eq.(A.1.4) then becomes,

$$\frac{e^2}{4\pi^3\hbar^2}\frac{\cos\theta}{1-\exp(-2\pi/\omega\tau)}\frac{m^*}{\omega}\frac{\pi}{a}\frac{4t^2a^2}{\hbar^2}$$
$$\times\sum_{\nu=-\infty}^{\infty}\sum_{\nu'=-\infty}^{\infty}\Big\{J_\nu(ak_F\tan\theta)J_{\nu'}(ak_F\tan\theta)$$
$$\times2\pi\delta_{\nu,\nu'}\frac{1/\omega\tau}{\nu'^2+(1/\omega\tau)^2}(1-\mathrm{e}^{-2\pi/\omega\tau})\Big\}$$
$$=\frac{2t^2am^*e^2\tau\cos\theta}{\pi\hbar^4}\sum_{\nu=-\infty}^{\infty}J_\nu(ak_F\tan\theta)^2\frac{1}{(\omega\tau\nu)^2+1.} \qquad (A.1.7)$$

Using $m^*\approx m/\cos\theta$, and hence, $\omega\tau\approx\omega_0\cos\theta$, the final result is given by

$$\sigma_{zz}=\sigma^0_{zz}\Big\{J_0^2(A)+2\sum_{\nu=1}^{\infty}\frac{J_\nu^2(A)}{1+(\omega_0\tau\nu\cos\theta)^2}\Big\} \quad , \qquad (A.1.8)$$

where $A=ak_F\tan\theta$, and the zero field conductivity σ^0_{zz} is given by eq.(2.5.15).

Appendix A.2 Bessel Functions

The generating function of Bessel functions is

$$e^{iz\sin\varphi} = \sum_{\nu=-\infty}^{+\infty} J_\nu(z)e^{i\nu\varphi}. \qquad (A.2.1)$$

since $\sin(\varphi + \frac{\pi}{2}) = \cos(\varphi)$, we obtain

$$e^{iz\cos\varphi} = \sum_{\nu=-\infty}^{+\infty} J_\nu(z)e^{i\nu(\varphi+\frac{\pi}{2})} \quad . \qquad (A.2.2)$$

Separation of the real and the imaginary parts yields,

$$\sin(z\cos\varphi) = \sum_{\nu=-\infty}^{+\infty} J_\nu(z)\sin(\nu(\varphi+\frac{\pi}{2})), \qquad (A.2.3)$$

$$\cos(z\cos\varphi) = \sum_{\nu=-\infty}^{+\infty} J_\nu(z)\cos(\nu(\varphi+\frac{\pi}{2})). \qquad (A.2.4)$$

Appendix A.3 Approximation

A.3.1 Approximation of k

We consider a corrugated cylindrical Fermi surface whose energy dispersion is given by eq.(1.3.1). In the weak corrugation limit, $k = \sqrt{k_x^2 + k_y^2}$ can be written as

$$\begin{aligned} k &\approx k_F(1 + \frac{t}{E_F}\cos(ak_z)) \\ &\sim k_F \times \Big\{1 + O(t/E_F)\Big\}. \end{aligned} \qquad (A.3.1)$$

A.3.2 Approximation of $v_\perp$

Next we approximate $\vec{v}_\perp = (v_{x\perp}, v_{y\perp}, v_{z\perp})$. It can be expressed by the following equation

$$\vec{v}_\perp = \vec{v} - (\vec{v}\cdot\vec{n})\cdot\vec{n}, \qquad (A.3.2)$$

where $\vec{n}$ is the unit vector $\vec{n} = (\sin\theta, 0, \cos\theta)$ in the direction of the magnetic field. Then $v_\perp$ is written as follows:

$$\begin{aligned} v_\perp = |\vec{v}_\perp| &= \sqrt{v_{x\perp}^2 + v_{y\perp}^2 + v_{z\perp}^2} \\ &= \sqrt{(v_x\cos\theta - v_z\sin\theta)^2 + v_y^2} \\ &\approx \sqrt{v_x^2\cos^2\theta + v_y^2} \times (1 + O(\tilde{v}_z/v_F)) \\ &\approx \sqrt{v_F^2\cos^2\xi\cos^2\theta + v_F^2\sin^2\xi} \\ &\qquad \times \{1 + O(\tilde{v}_z/v_F) + O(t/E_F)\}. \end{aligned} \qquad (A.3.3)$$

Here, $\tilde{v}_z = 2ta/\hbar$.

A.3.3 Approximation of $dk_\parallel$

The definition of $dk_\parallel$ is

$$dk_\parallel = \sqrt{dk_x^2 + dk_y^2 + dk_z^2}. \qquad (A.3.4)$$

Differentiating eq.(2.3.1) we obtain $dk_z = -\tan\theta dk_x$. Then eq.(A.3.4) is

$$\begin{aligned} dk_\parallel &= \sqrt{(1+\tan^2\theta)dk_x^2 + dk_y^2} \\ &= \frac{1}{\cos\theta}\sqrt{dk_x^2 + \cos^2\theta dk_y^2}. \end{aligned} \qquad (A.3.5)$$

Using the polar coordinates (k,ξ), dk_x and dk_y are

$$dk_x = \cos\xi dk - k\sin\xi d\xi \qquad (A.3.6)$$

$$dk_y = \sin\xi dk + k\cos\xi d\xi. \qquad (A.3.7)$$

The relation between dk and $d\xi$ can be derived by differentiating eq.(1.3.1) with $E = E_F$.

$$\begin{aligned} dk &= \frac{2ta\sin(ak_0 - ak\tan\theta\cos\xi)k\tan\theta\sin\xi d\xi}{-\hbar^2 k/m + 2ta\sin(a(k_0 - k\tan\theta\cos\xi))\tan\theta\cos\xi} \\ &\sim d\xi\left\{-\frac{m}{\hbar}v_z\tan\theta\sin\xi\right\} \times \left\{1 + O(\tilde{v}_z\tan\theta/v_F)\right\} \\ &\sim -d\xi k_F\left(\frac{v_z\tan\theta}{v_F}\right)\sin\xi \times \left\{1 + O(\tilde{v}_z\tan\theta/v_F)\right\}. \end{aligned} \qquad (A.3.8)$$

Using the above equation, eq.(A.3.6),(A.3.7) becomes

$$dk_x \sim d\xi\left\{-k_F\sin\xi + k_F\cdot O(t/E_F) + k_F\cdot O(\tilde{v}_z\tan\theta/v_F)\right\} \qquad (A.3.9)$$

$$dk_y \sim d\xi\left\{k_F\cos\xi + k_F\cdot O(t/E_F) + k_F\cdot O(\tilde{v}_z\tan\theta/v_F)\right\}. \qquad (A.3.10)$$

Substitution of these relations into eq.(A.3.5) yields

$$dk_\parallel = d\xi\left\{\frac{k_F}{\cos\theta}\sqrt{\sin^2\xi + \cos^2\theta\cos^2\xi}\right\} \times \left\{1 + O(t/E_F) + O(\tilde{v}_z\tan\theta/v_F)\right\}. \qquad (A.3.11)$$

A.3.4 Approximation of m^* and φ

Using the relation derived in Secs. A.3.1-A.3.3, the cyclotron mass is approximated by

$$m^* \equiv \frac{\hbar}{2\pi}\oint\frac{dk_\parallel}{v_\perp} \sim \frac{m}{\cos\theta} \times \left\{1 + O(t/E_F) + O(\tilde{v}_z/v_F) + O(\tilde{v}_z\tan\theta/v_F)\right\}, \qquad (A.3.13)$$

and the phase variable is

$$d\varphi = \frac{\hbar}{m^*}\frac{dk_\parallel}{v_\perp} \sim d\xi \times \left\{1 + O(t/E_F) + O(\tilde{v}_z/v_F) + O(\tilde{v}_z\tan\theta/v_F)\right\}. \qquad (A.3.14)$$

Thus we can approximate the phase variable φ by ξ. It is manifest from the above discussion that the explicit equality holds between ξ and φ when $t/E_F = 0$.

Appendix B

Cusp in the Angular Dependence of the Magnetoresistance in GaAs/AlGaAs Superlattice

Measurements of magnetoresistance as a function of field angle in $GaAs/Al_xGa_{1-x}As$ superlattices have revealed a cusp-like structure when the magnetic field is parallel to the layer plane. We show that this cusp-like structure results from the anisotropy of negative magnetoresistance possibly due to localization effect rather than the divergent semi-classical magnetoresistance due to the open orbit of Fermi surface. The relation between the cusp-like structure and the Fermi surface topology is also discussed.

B.1 Introduction

During the course of our study of the angular dependent magnetotransport in $GaAs/Al_xGa_{1-x}As$ superlattice, we have found that the resistance as a function of magnetic field angle exhibits a characteristic cusp-like structure when the field is parallel to the basal plane. In this Appendix, we report on our detailed study of this cusp-like structure.

B.2 Experimental

Three different samples of $GaAs/Al_xGa_{1-x}As$ superlattice have been grown by MBE. The relevant parameters for the three superlattices are summarized in Table B.1. The schematic diagram of the band structure and the Fermi surface shape are illustrated in Fig.B.1. The parameters for Device A were so chosen that it had a quasi-two-dimensional (*i.e.* cylindrical) Fermi surface. (This is the same sample as "Device L_1 " in Chapter 3.) In Device B, the total carrier density was approximately the same as Device A, but the thickness of the $Al_xGa_{1-x}As$ barrier layer was reduced. The size of the Brillouin zone

Device I.D.	*A*	*B*	*C*
GaAs layer thickness [Å]	100	62	64
$Al_xGa_{1-x}As$ layer thickness [Å]	60	23	24
Number of periods	100	50	100
Alloy composition x	0.154	0.25	0.25
Carrier density $n_H[cm^{-3}] \times 10^{17}$	4.6	4.0	33
Ground subband width [meV]	6	43	40
First mini-gap width [meV]	50	83	80
Fermi level [meV]	29	27	116
Fermi surface topology	2D	3D	2D
Hall mobility (4.2K) $[cm^2/Vs]$	2370	1810	1890

Table B.1 Superlattice device parameters.

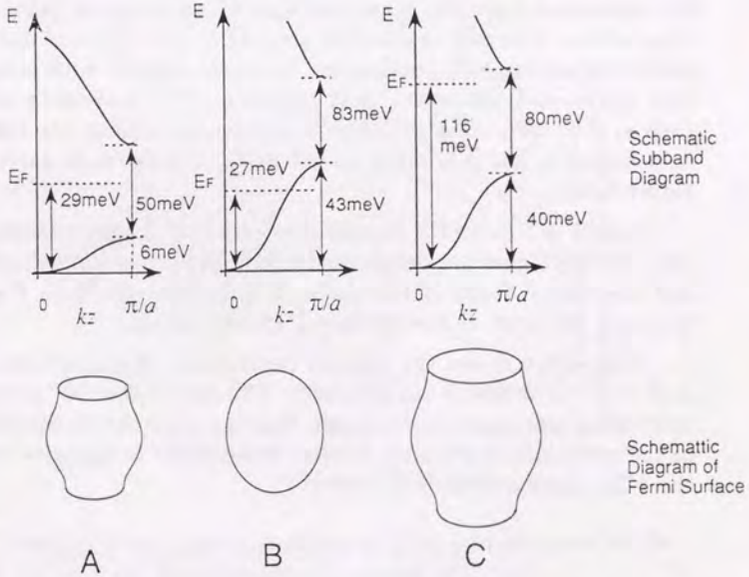

Fig. B.1 Schematic diagram of the subband structure and the Fermi surface shape.

in the k_z-direction was accordingly larger, and the Fermi surface was closed within the first Brillouin zone. In Device C, the superlattice structure was made the same as Device B, but the total carrier density was increased so that the Fermi surface became extended in the k_z-direction.

Details of the sample fabrication and the magnetotransport measurements were described in Chapter 3.

B.3 Results and Discussion

First we describe the cusp-like structure observed in the angular dependence of magnetoresistance in Device A.

B.3.1 Cusp-Like Feature at $\theta = 90°$

Figure B.2 shows the angular dependence of magnetoresistance in Device A for different field intensities at $T = 4.2$K. The field angle θ is measured from the normal of the two-dimensional plane of the superlattice. The SdH oscillations are seen in the high field data. The amplitude of the SdH oscillations decreases rapidly with increasing field angle, and decreasing field intensity. The resistance shows a cusp at $\theta = 90°$. The cusp-like structure depends on the magnetic field strength, *i.e.* it is broad at low fields, and becomes narrower at higher fields.

Figure B.3 shows the angular dependence of magnetoresistance at 44K. At this higher temperature, the SdH amplitude is much reduced, and the overall shape of the curves is quite different from Fig. B.2. However, the cusp at $\theta = 90°$ is still clearly visible.

Figure B.4 shows the angular dependence of magnetoresistance at $B = 9$T for different temperatures. The cusp at $\theta = 90°$ grows with decreasing temperature. It is seen that ignoring the oscillatory part of the resistance the overall angular dependence is opposite between the 4.2K curve and the 61K curve.

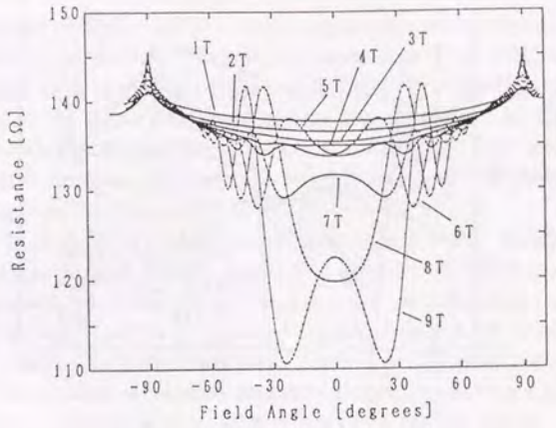

Fig.B.2 Angular dependence of magnetoresistance of Device A for different field intensities. $T = 4.2$K.

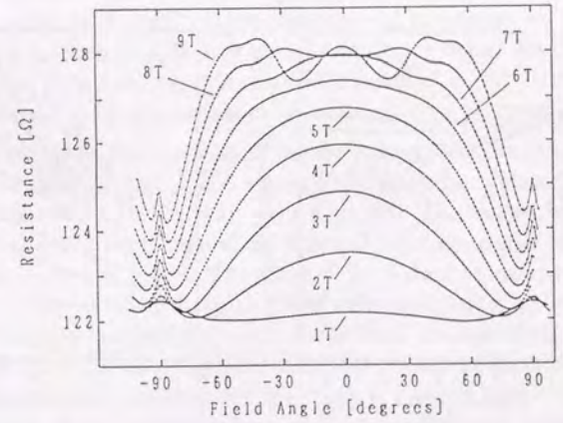

Fig.B.3 Angular dependence of magnetoresistance of Device A for different field intensities. $T = 44$K.

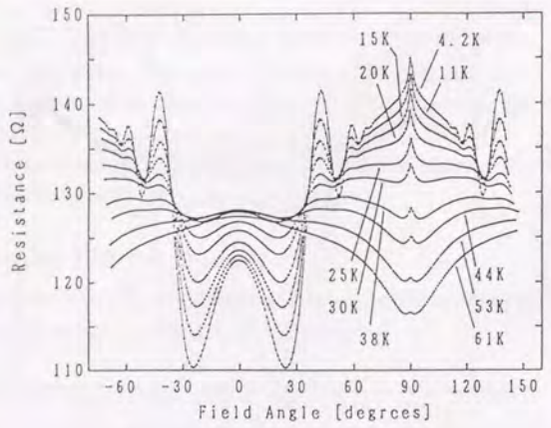

Fig. B.4 Angular dependence of magnetoresistance of Device A for different temperatures. $B = 9$T.

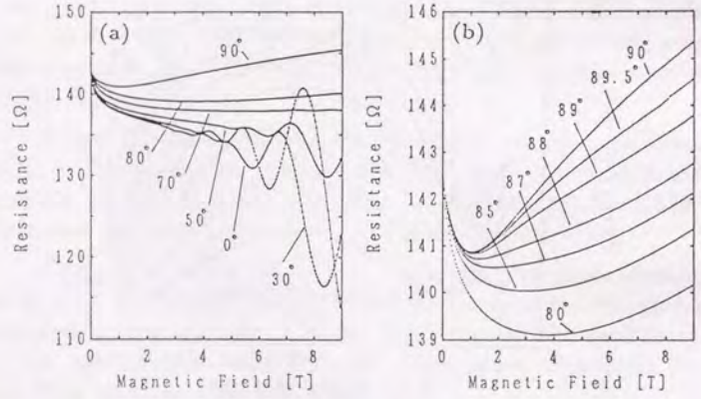

Fig. B.5 (a) Field dependence of resistance of Device A for different field angles. $T = 4.2$K. (b) Detailed field dependence of resistance of Device A around $\theta = 90°$. $T = 4.2$K.

B.3.2 Field Dependence

Next we look at the magnetoresistance as a function of magnetic field. Figure B.5(a) shows the magnetoresistance at $T = 4.2$K at different field angles as a function of magnetic field. For field angles not too close to $\theta = 90°$, the SdH oscillations are observed. In the low field regime, negative magnetoresistance is observed. The magnitude of the negative magnetoresistance is largest at $\theta = 0°$. It decreases with increasing field angle toward $\theta = 90°$.

The high field asymptotic behavior near $\theta = 90°$ is different from other angles. Figure B.5(b) shows the detailed measurement of magnetoresistance between $\theta = 90°$ and $\theta = 80°$ as a function of magnetic field. At $\theta = 90°$, a large positive magnetoresistance is observed for $B > 1$T. As the field is tilted away from $\theta = 90°$ positive magnetoresistance diminishes while the negative magnetoresistance grows so the resistance minimum occurs at progressively higher fields.

B.3.3 Origin of the Cusp-Like Feature

One of the candidates for the origin of the cusp is the appearance of an open orbit at $\theta = 90°$. It is quite natural to expect an open orbit along the k_z-direction in our quasi-two-dimensional Fermi surface. Indeed, the high field asymptotic behavior at $\theta = 90°$ is reminiscent of a divergent magnetoresistance associated with an open orbit.

However, the explanation in terms of an open orbit runs into difficulty. The inset of Figure B.6 shows the detailed angular dependence of the data shown in Fig. B.3 near $\theta = 90°$. The cusp-like structure becomes sharper with increasing field. The main panel of Fig. B.6 shows the replot of Fig. B.3 as a function of field component perpendicular to the two-dimensional plane of superlattice($B_\perp = B\cos\theta$). Aside from the vertical shift, all curves look similar to one another. Thus the shape of the cusp-like structure is determined only by the perpendicular field component $B_\perp$. On the other hand the vertical shift of each curve is determined by the total field intensity.

From these results, the same positive magnetoresistance as that at $\theta = 90°$ also exists at other field angles. Therefore, it cannot be attributed to an open orbit, because the open orbit only exists in the vicinity of $\theta = 90°$.

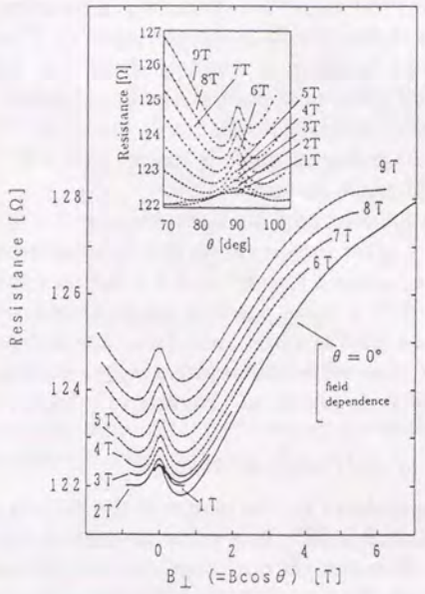

Fig. B.6 The scaled plot of the angular dependence of magnetoresistance of Device A as a function of $B\cos\theta$. $T = 44$K. Field dependence at $\theta = 0$ is plotted together for comparison. The inset is the detailed angular dependence of magnetoresistance around $\theta = 90°$. $T = 44$K.

From the scaled plot of Fig. B.6, it is evident that the angular dependence for a fixed field intensity basically reflects the field dependence at $\theta = 0°$. The negative magnetoresistance and the resistance minimum of the field dependence correspond to the cusp-like feature and to the resistance minimum of the field angle dependence, respectively. We conclude that the cusp-like structure arises from the negative magnetoresistance which is solely determined by the perpendicular component of the magnetic field.

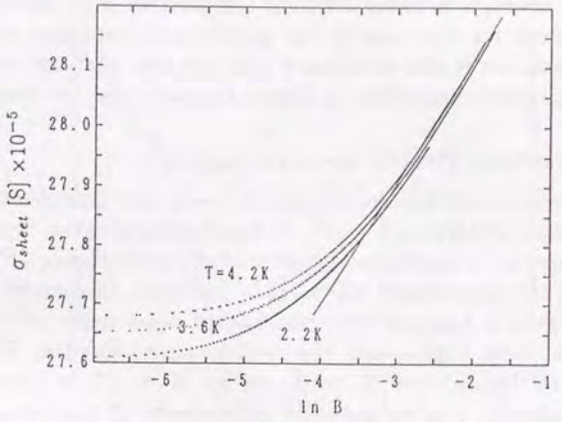

Fig.B.7 Plot of the conductivity of Device A for one superlattice layer vs. lnB.

B.3.4 Negative Magnetoresistance

Next we discuss the origin of the negative magnetoresistance. We first exclude the effect arising from the magnetic impurity such as a Kondo effect because the MBE machine as well as the deposition sources used in the superlattice growth are clean enough to make a GaAs/AlGaAs heterostructure two-dimensional electron gas whose mobility exceeds 1×10^6 cm^2/Vsec. The most probable candidates for the origin of the negative magnetoresistance is the weak localization effect widely seen in semiconductors.

Fig. B.7 shows a plot of the magneto-conductivity $\Delta\sigma_{sheet}$ v.s. lnB, where σ_{sheet} is the conductivity of Device A for one superlattice layer. The magnetoconductivity is linear in lnB for $B > 0.05$T, which can be described as $\delta(\Delta\sigma) = \alpha(e^2/2\pi^2\hbar)lnB$, with α=0.19.

We are aware of that the present analysis is rough. The results however strongly suggest that the negative magnetoresistance is due to a weak localization effect. We do not further concern with the origin of the negative magnetoresistance since it is irrelevant to the main subject in this thesis.

If we consider the negative magnetoresistance is due to the localization effect, it is natural that it is scaled by the perpendicular field component for the case of the quasi-two-dimensional system. The interpretation is also consistent with the fact that the negative magnetoresistance diminishes at higher temperatures, so does the cusp.

B.3.5 Isotropic Positive Magnetoresistance

We have pointed out the distinct temperature dependence of positive magnetoresistance at $\theta = 90°$. It might seem possible to associate the field angular independent positive magnetoresistance to the Zeeman part of the localization effect. This, however, encounters a difficulty.

Figure B.8 shows the temperature dependence of resistance for different field angles with the field intensity fixed at 9T. The temperature dependence of resistance at $B = 0$T is also plotted for comparison†. The temperature dependence of magnetoresistance at $B = 9$T,$\theta = 90°$ is similar to that at zero field, as seen in Fig. B.8. Therefore, it is difficult to attribute the positive magnetoresistance at $\theta = 90°$, which survives up to $T \sim 200$K, to the localization effect. We have not obtained a clear explanation of the temperature independent isotropic magnetoresistance observed at $\theta = 90°$.

B.4. Fermi Surface Topology and the Cusp-Like Feature

In case of Device A, cusp-like structure of the angular dependence arises from anisotropy of the localization effect, and the shape is determined by $B_\perp = B\cos\theta$. We compare these results with two other Devices B and C.

Device B has the same carrier density as Device A, but a larger 1D subband width. The Fermi level of Device B falls in the 1D subband. As a consequence, the Fermi surface of Device B is closed within the first Brillouin zone. This is seen from the fact that SdH oscillations are observed for all field angles, as seen in Fig. B.9(b). Figure B.9(a) shows the angular dependence of magnetoresistance for Device B at different field intensities. The shape of the curves of the angular dependence is quite different from Device A. What draws our attention is that there is no cusp-like feature at $\theta = 90°$ in this sample. We also note that positive magnetoresistance is not observed even at $\theta = 90°$,

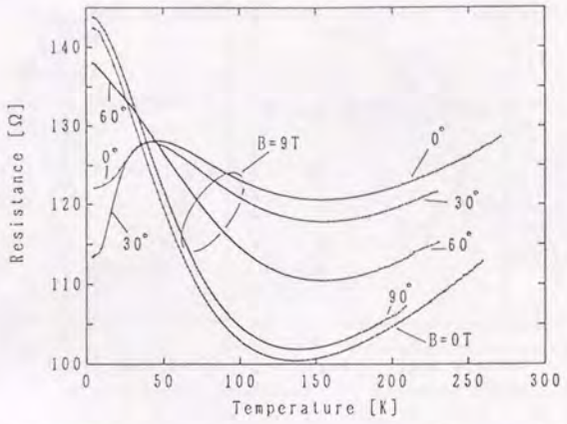

Fig.B.8 Temperature dependence of resistance of Device A for different field angles. $B = 9$T. Zero field resistance is plotted for comparison.

i.e. the non-oscillatory part of the magnetoresistance is negative at all angles.

Device C has an identical superlattice structure as Device B. But its electron density is about eight times as high as that of Device B. The Fermi surface of Device C touches the Brillouin zone boundary in the k_z-direction. Namely the Fermi surface is cylindrical and topologically similar to Device A.

Figure B.10(a) shows the angular dependence of magnetoresistance for Device C at different field intensities. The general shape of the curves is the same as Device A. There is an oscillatory magnetoresistance around $\theta = 0°$. It diminishes with increasing field angle. The oscillatory change of magnetoresistance with angle is also due to the SdH effect. A cusp-like structure at $\theta = 90°$ similar to that observed in Device A is seen . Figure B.10(b) is the magnetoresistance as a function of magnetic field at different field angles. At $\theta = 90°$, where the cusp occurs, the positive magnetoresistance is seen.

From these results, we could see that the cusp at $\theta = 90°$ has

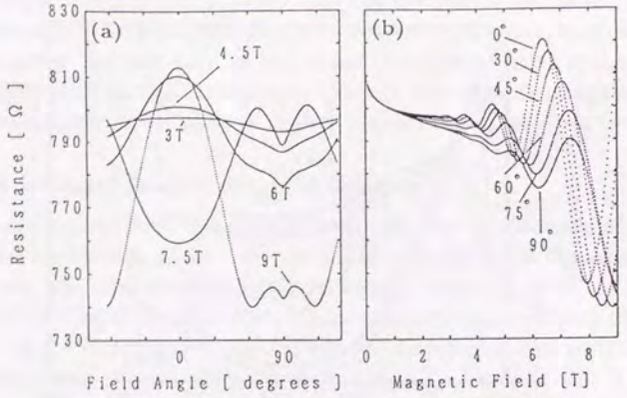

Fig. B.9 (a) Angular dependence of magnetoresistance of Device B for different field angles.$T = 4.2$K. (b) Field dependence of magnetoresistance of Device B for different field angles. $T = 4.2$K.

relevance to the quasi-two-dimensional Fermi surface. This effect is commonly observed in Devices A and C, both of which have cylindrical Fermi surface albeit with widely different electron densities.

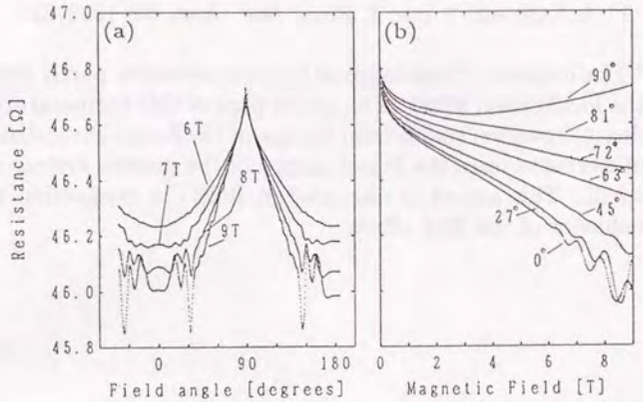

Fig. B.10 (a) Angular dependence of magnetoresistance of Device C for different field angles. $T = 1.3$K. (b) Field dependence of magnetoresistance of Device C for different field angles. $T = 1.3$K.

B.5.Conclusion

During the course of the study of the angular dependent magnetoresistance oscillation effect, we have found the anomalous cusp-like structure at $\theta = 90°$ in the lateral transport of GaAs/Al_xGa_{1-x}As superlattice. We have characterized the cusp-like structure as follows:

1) The cusp-like structure is manifest especially in low temperature regime, and disappears gradually at higher temperatures.
2) It accompanies positive magnetoresistance in high field regime.
3) Its angular dependence can be scaled by the perpendicular field component, $B\cos\theta$.

We attribute the cusp-like structure to the anisotropy of the negative magnetoresistance arising from the localization effect. It is demonstrated that the appearance of this cusp is correlated with the Fermi surface topology.

References

1) R.Yagi and Y.Iye: J. Phys. Soc. Jpn., **61**(1992)227.

† The increase of resistance at low temperatures partly stems from the localization effect. The major part of this temperature dependence, however, comes from change in the Fermi-Dirac distribution of electrons since the Fermi energy in the present system is rather small. This aspect is discussed in Ref[1] in connection with the behavior of the Hall effect.

169